Mechanosensation of tight junctions by ZO-1 phase separation and flow

Cornelia Schwayer[1], Shayan Shamipour[1], Kornelija Pranjic-Ferscha[1], Alexandra Schauer[1], Maria Balda[3], Masazumi Tada[2], Karl Matter[3] and Carl-Philipp Heisenberg[1,4*]

[1] Institute of Science and Technology Austria, Klosterneuburg, Austria

[2] Department of Cell and Developmental Biology, University College London, London, UK

[3] Institute of Ophthalmology, University College London, London, UK

[4] Lead Contact

* Correspondence: heisenberg@ist.ac.at

Summary

Cell-cell junctions respond to mechanical forces by changing their organization and function. Tension-dependent conformational changes of junctional proteins are thought to underlie this junctional mechanosensitivity. Here we show that in the gastrulating zebrafish embryo, tight junction (TJ) mechanosensitivity is mediated by actomyosin-driven flow of phase separated Zonula occludens-1 (ZO-1) clusters. We found that ZO-1 junctional accumulation at the contact between the Enveloping Layer (EVL) and the Yolk Syncytial Layer (YSL) closely scales with actomyosin tension. Actomyosin tension triggers ZO-1 junctional accumulation by driving retrograde actomyosin flow within the YSL that transport non-junctional ZO-1 clusters towards the TJ. Non-junctional ZO-1 clusters form by phase separation, and direct binding of ZO-1 to actin is required for stable incorporation of ZO-1 clusters into TJ. If the formation and/or junctional incorporation of ZO-1 clusters is impaired, TJ lose their mechanosensitivity, and, consequently, EVL-YSL movement is delayed. Thus, phase separation and flow of non-junctional ZO-1 confer mechanosensitivity to TJ.

Introduction

A key step in the emergence of multicellularity is the development of different junctional complexes mechanically connecting cells and allowing the transfer of biochemical and mechanical signals between cells. The molecular composition and dynamic regulation of different cell-cell junction types, such as adherens junctions (AJ), tight junctions (TJ) and desmosomes, have been extensively studied over the past decades (Franke, 2009; Godsel et al., 2004; Niessen, 2007; Van Itallie and Anderson, 2014). Likewise, detailed insight has been gained in the intracellular signaling cascades activated by the different junctional complexes and their function in tissue homeostasis (Johnson et al., 2014; Matter and Balda, 2003;

Wheelock and Johnson, 2003; Zihni et al., 2016). There is also compelling evidence that changes in the molecular composition, size and turnover of junctional complexes directly affect both their mechanical integrity and signaling activity (Baum and Georgiou, 2011; Cunningham and Turner, 2012; Nekrasova and Green, 2013; Shen et al., 2008). In contrast, much less is known about how mechanical forces influence cell-cell junction formation and signaling.

Recent studies on AJ indicate that mechanical forces and actin dynamics at E-cadherin-mediated cell-cell contacts can promote E-cadherin clustering, leading to the formation of larger and more stable junctional complexes (Cavey and Lecuit, 2009; Cavey et al., 2008; Engl et al., 2014; Ladoux et al., 2010). An important step in this mechanosensing process is the modulation of AJ anchoring to the cortical actomyosin network, with junctional tension changing the conformation of AJ components, such as α-catenin and vinculin, thereby increasing their binding capacity to the actomyosin network (Gomez et al., 2011; Watabe-Uchida et al., 1998; Weiss et al., 1998; Yonemura et al., 2010). Tension-dependent changes in the composition and organization of AJ are thought to affect both their coupling strength and signaling activity (Gomez et al., 2011). While recent studies suggest that certain components of other junction types, such as TJ, can in principle undergo conformational changes upon mechanical loading (Spadaro et al., 2017), it is not yet entirely clear whether and how this molecular mechanosensitivity translates into changes of global junction organization and function.

TJ play an essential role in tissue homeostasis by limiting the passage of molecules and ions between cells and restricting the movement of molecules between the apical and basolateral domains thereby maintaining apicobasal polarity of epithelial cells (Shin et al., 2006). Similar to AJ, TJ are composed of transmembrane proteins, such as Occludins and Claudins and cytoplasmic scaffolding proteins connecting the transmembrane proteins to the cytoskeleton, such as Zonula Occludens (ZO) proteins and Cingulins (Zihni et al., 2016). TJ also function as intracellular signaling centers regulating the activity of small Rho GTPases, such as RhoA and Cdc42, thereby affecting actomyosin network organization and contraction at the junction (Zihni and Terry, 2015). Conversely, actomyosin regulators such as RhoA, Cdc42 and Rac have been shown to be important for TJ formation (Zihni et al., 2016); yet, to what extent mechanical signals, for instance by triggering conformational

changes of TJ components (Spadaro et al., 2017), are involved in this process still needs to be established.

During zebrafish epiboly, the enveloping cell layer (EVL), a simple squamous epithelial monolayer covering the blastoderm at the animal pole of the yolk cell, spreads together with the underlying deep cells over the entire yolk cell (Figure 1A; (Behrndt et al., 2012; Cheng et al., 2004; Holloway et al., 2009; Köppen et al., 2006). EVL spreading is driven by a large actomyosin ring-like structure positioned within the yolk syncytial layer (YSL) on the surface of the yolk cell and coupled to the EVL leading edge by both AJ and TJ (Figure 1A; (Köppen et al., 2006). The actomyosin ring drives EVL spreading by actively pulling on the EVL-leading edge through two distinct motor-activities: (i) a cable-constriction motor, where the actomyosin band constricts around its circumference, thereby generating pulling forces on the EVL margin once the band has crossed the yolk cell equator; and (ii) a flow-friction motor, where a gradient of actomyosin tension along the width of the actomyosin band gives rise to retrograde actomyosin flow. This actomyosin flow, when resisted by friction to adjacent structures within the YSL, will generate a traction force pulling the EVL margin towards the vegetal pole (Behrndt et al., 2012). The pulling forces generated by the actomyosin band within the YSL are likely transmitted to the margin of the EVL by junctional complexes connecting the leading edge of the EVL to the YSL (Behrndt et al., 2012; Köppen et al., 2006). Whether and how junction formation at the EVL-YSL boundary relates to actomyosin ring formation and function within the YSL is still unknown.

Here, we show that TJ rather than AJ components accumulate at the EVL-YSL boundary during the course of EVL epiboly, and that this accumulation closely scales with the degree of actomyosin tension within the YSL. We further show that the accumulation of TJ components at the EVL-YSL boundary is mediated by tension-dependent retrograde actomyosin flow within the YSL transporting non-junctional phase separated ZO-1b towards the boundary. Finally, we show that this mechanosensitive response of TJ at the EVL-YSL junction is required for proper EVL spreading.

Results

Tight junction components accumulate at the EVL-YSL boundary

We have previously noted that both AJ and TJ components localize to the boundaries between EVL cells and at the leading edge of the EVL where it contacts the YSL (Köppen et al., 2006). To investigate which junctions form at the EVL-YSL boundary during the course of EVL epiboly, we systematically analyzed how the localization of various AJ and TJ components changes during epiboly. Interestingly, we found that the accumulation of components typically associated with AJ, such as E-cadherin, α-catenin and β-catenin, decreased at the EVL-YSL boundary during epiboly (Figures 1A-D and S1A-D). In contrast, the accumulation of various components typically associated with TJ either increased (ZO-1b, Cingulin-like 1) or remained unchanged (ZO-3, Claudin-D and Occludin-A) at this boundary during epiboly (Figures 1A-D and S1A-D). This suggests that during the course of EVL epiboly, TJ becomes the predominant junction type connecting the EVL leading edge to the YSL.

ZO-1b and ZO-3 are required for proper EVL epiboly movements by regulating actomyosin flow and tension within the YSL

To determine whether this accumulation of TJ components at the EVL-YSL boundary during epiboly is functionally relevant for EVL epiboly movements, we sought to interfere with the expression of those components and analyze resultant changes in EVL epiboly movements. Given the known signaling function of TJ in regulating actin network organization and contraction (Zihni and Terry, 2015), we speculated that TJ might function in EVL epiboly movements by controlling actomyosin ring formation and flow within the YSL, previously shown to drive EVL epiboly movements (Behrndt et al., 2012). To test this possibility, we injected *morpholinos* (MO) directed against the TJ components *zo-1b* and *zo-3,* previously implicated in TJ organization and signaling to the actomyosin cytoskeleton (Itoh et al., 2012; Otani et al., 2006; Tornavaca et al., 2015; Wittchen et al., 2003), directly into the YSL to specifically interfere with ZO-1b/3 expression at the EVL-YSL boundary (Figure 2A). YSL-morphant embryos displayed clearly reduced EVL epiboly movements, which could be partially rescued by co-injecting GFP-tagged *zo-1b and zo-3* mRNA (Figure 2A-A'', Movie 1). In contrast, injection of *zo-1b* and *zo-3* mismatch MOs or a standard negative control MO into the YSL did not elicit a recognizable epiboly phenotype (Figure S2A), supporting the specificity of the *zo-1b/3* morphant phenotype. The slower EVL spreading phenotype was accompanied by diminished retrograde actomyosin flow and ring formation within the YSL (Figure 2C-C',D-D', Movies 3 and 4), a phenotype that could be partially rescued by co-injecting GFP-tagged *zo-1b and zo-3* mRNA (Figures 2C-C',D-D'). Notably, the epiboly phenotype in *zo1b/3* morphant embryos was not due to a general developmental delay, as

YSL morphant embryos formed the first somite, visualized by *papc* expression, at the same time as their control injected siblings (Figure S2B-B'). Likewise, when *zo1b/3* was ubiquitously knocked down or knocked out (MZ*zo1b/3* mutants), the large majority of morphant or mutant embryos formed the first somite on time (Figure S2C-C'). Together, these observations suggest that TJ formation at the EVL-YSL boundary is required for EVL epiboly movements by regulating actomyosin flow and ring formation within the YSL.

To determine whether the obtained morphant phenotypes were specific, we generated maternal-zygotic (MZ) mutants for the TJ components ZO-1b and ZO-3, using CRISPR/Cas9 technique (Figure S2D). We found that while in MZ*zo-1b* and MZ*zo-3* single mutants, EVL spreading appeared largely unaffected (Figure S2E), MZ*zo-1b/3* double mutants displayed a phenotype closely resembling the phenotypes observed in embryos where ZO-1b and ZO-3 expression was knocked down either uniformly or locally within the YSL using MOs (Figures 2B-B'', A-A'' and S2G'', Movie 2). The phenotypic similarities between mutant and morphant embryos further suggest that the obtained *zo-1b/3* morphant phenotypes were specific and, thus, that the *zo-1b* and *zo-3* MOs can be used to analyze the function of those proteins in EVL-YSL epiboly. Notably, TJ were reduced but not completely absent at the EVL-YSL boundary in *zo-1b/3* YSL morphants (Figure S2F-F') and mutants (Figure S2G-G'), likely due to incomplete knockdown in morphant embryos and functional redundancy and/or compensatory upregulation in the expression of the remaining *zo* genes (*zo-1a, zo-2a, zo-2b*) in mutant embryos (Figure S2H).

To understand how TJ components accumulate at the EVL-YSL boundary during the course of epiboly, we asked which changes at the EVL-YSL boundary might coincide with this accumulation. We have previously shown that actomyosin network tension and retrograde flow within the YSL increases during EVL epiboly (Behrndt et al., 2012). We thus reasoned that the accumulation of TJ components at the EVL-YSL junction might coincide with actomyosin-mediated tension increase at this boundary. To address this possibility, we determined tension at the EVL-YSL boundary oriented along the circumference of the yolk cell at mid (6 hpf) and late (8 hpf) stages of epiboly using UV-laser ablation. Consistent with our previous analysis of the evolution of actomyosin network tension within the YSL during epiboly (Behrndt et al., 2012), we found that tension at the EVL-YSL junction of wild type (WT) embryos was considerably higher at late compared to early stages of epiboly (Figures 2E-E'' and S2I-I', Movie 5). In contrast, junctional tension was strongly reduced in *zo-1b/3*

YSL morphant embryos at late stages of epiboly (Figures 2F-F'' and S2J-J', Movie 6), indicating that normal TJ formation is required for proper buildup of tension at the EVL-YSL junction. Together, this spatiotemporal correlation between TJ component accumulation and junctional tension at the EVL-YSL boundary point at the possibility that junctional tension might be involved in TJ formation and maturation at this boundary.

Actomyosin contractility controls ZO-1 recruitment to the EVL-YSL boundary

To determine whether and how increased junctional tension at the EVL-YSL boundary relates to TJ formation at this boundary, we sought to modulate actomyosin contractility within the YSL and determine resultant effects on TJ formation at the EVL-YSL boundary. To modulate actomyosin contractility specifically within the YSL, we performed YSL-injections of mRNAs encoding constitutive active (ca) versions of either Myosin Phosphatase (caMypt) (Jayashankar et al., 2013; Smutny et al., 2017) or RhoA (caRhoA) (Takesono et al., 2012), previously shown to decrease or increase actomyosin contractility, respectively. Strikingly, we found that in embryos with reduced actomyosin contractility and retrograde flow rates within the YSL (Figures S3A-A',B-B' and 2C-C',D-D'), the accumulation of TJ components, and in particular of ZO-1b, at the EVL-YSL boundary was clearly reduced (Figure 3A-A''). Conversely, ZO-1b at the EVL-YSL boundary showed a premature and strong accumulation in embryos with increased actomyosin contractility and retrograde flow rates within the YSL (Figures 3B-B'' and S3C-C',D-D'). AJ components, in contrast, did not display any recognizable changes in response to altered actomyosin tension at the EVL-YSL junction (Figure S3E-E'). Collectively, these findings indicate that actomyosin network contractility and retrograde flow within the YSL triggers TJ component accumulation at the EVL-YSL boundary, suggesting that TJ at this boundary are mechanosensitive.

Non-junctional clusters of ZO-1b within the YSL undergo retrograde flows and are incorporated into TJ at the EVL-YSL boundary

To understand how actomyosin network tension translates into the accumulation of TJ components at the EVL-YSL boundary, we performed high-resolution time-lapse imaging of ZO-1b accumulation at the EVL-YSL boundary at 7 hpf. Remarkably, we detected non-junctional clusters of ZO-1b within the YSL close to the EVL-YSL boundary, which flew at a similar velocity as the actomyosin network towards this boundary (Figure 4A-A'',B-B'', Movies 7 and 8). ZO-1b clusters arriving at the EVL-YSL boundary were then incorporated into the junction, thereby locally increasing the amount of ZO-1b at the junction (Figure 4C-

C', Movie 9). Closer analysis of these non-junctional ZO-1b clusters showed that ZO-1b close to the EVL-YSL boundary displayed a tendency to fuse into larger clusters (Figure 4D-D''), Movie 10). Given that fusion of protein clusters or 'droplets' has previously been associated with protein phase separation (Brangwynne et al., 2009; Li et al., 2012), this points at the intriguing possibility that non-junctional ZO-1b clusters within the YSL might form by phase separation. To form phase separated droplets, multivalent interactions on an intra- or inter-molecular level are necessary (Banani et al., 2017; Kato et al., 2012; Li et al., 2012). Indeed, ZO-1 can undergo multivalent interactions with other ZO proteins such as ZO-2 and ZO-3 as well as other TJ scaffolding proteins, such as Cingulins (Fanning et al., 1998, 2007; Utepbergenov et al., 2006). There is also evidence for intra-molecular interaction sites for ZO-1 and other members of the MAGUK (membrane-associated guanylate kinases) protein family (Ye et al., 2018); (Lye et al., 2010; Spadaro et al., 2017)(Ye et al., 2018). This suggests that ZO-1b might be capable of undergoing phase separation, and that this property might contribute to its previously demonstrated scaffolding function in recruiting other proteins to TJ (Bauer et al., 2010; Fanning and Anderson, 2009; Matter and Balda, 2003).

To test whether ZO-1b within the YSL shows further properties indicative of a phase separation process, we sought to analyze ZO-1b turnover in clusters adjacent to the EVL margin using FRAP (Fluorescence recovery after photobleaching). Based on previous observations that proteins undergoing liquid-liquid phase separation stay highly dynamic within phase separated droplets (Brangwynne et al., 2009; Hyman et al., 2014), we hypothesized that if ZO-1b would undergo phase separation within the YSL, then the turnover of the ZO-1b non-junctional pool should be rather fast. Consistent with ZO-1b potentially undergoing phase separation, we found that at early-mid gastrulation stages (5-6 hpf) non-junctional ZO-1b showed fast turnover on a second scale ($t_{1/2}$ fast = 4 sec) and almost all of it was mobile (99% mobile fraction) (Figure 4E-E''). Interestingly, non-junctional ZO-1b also exhibited turnover on a minute scale ($t_{1/2}$ slow = 140 sec) indicative of the presence of a second, slower ZO-1b species (Figure 4E-E''). Surprisingly, however, at later gastrulation stages (7-8 hpf), the turnover time of non-junctional ZO-1b during the fast phase ($t_{1/2}$ fast) increased (4 sec to 13 sec) and its mobile fraction decreased (from 99% to 64% mobile fraction) (Figure 4F-F''). This suggests that clusters of non-junctional ZO-1b within the YSL, initially displaying properties of liquid-liquid phase separated condensates, might undergo a maturation process leading to their immobilization. Interestingly, analyzing turnover of ZO-

1b directly at the EVL-YSL junction at early (5 hpf) and later stages of gastrulation (8 hpf) revealed an even smaller fraction (~40%) of mobile ZO-1b at both of these stages (Figure S4A-A'',B-B''), suggesting that junctional incorporation of ZO-1b might further promote its immobilization.

A likely feature of a thermodynamically driven phase separation process is the dependency on concentration. To test how the concentration of ZO-1b expressed within the YSL relates to cluster formation of ZO-1b, we analyzed the size and fusion rate of those clusters as a function of ZO-1b concentration within the YSL. We found that both the size and fusion rate of non-junctional clusters of ZO-1b linearly scaled with the concentration of ZO-1b expressed within the YSL (Figures 4G-G''' and S4C), demonstrating that cluster formation is dependent on ZO-1b concentration as expected for a phase separation mechanism.

Non-junctional ZO-1b undergoes phase separation within the YSL

Next, we sought to identify domains or regions within ZO-1b that are important for its presumed phase separation behavior. To this end, we first tested a C-terminally truncated version of ZO-1b (ZO-1bΔC) (Figure 5A), which has recently been found in *in vitro* reconstitution and cell culture assays to be defective in undergoing phase separation likely due to changes in intramolecular interactions of the truncated protein (Beutel et al.). Substituting full-length ZO-1b with ZO-1bΔC by expressing ZO-1bΔC in MZ*zo1b/3* mutant embryos revealed that ZO-1bΔC exclusively localized to TJ and was unable to form non-junctional clusters within the YSL (Figure 5B). This is consistent with the notion that non-junctional ZO-1b clusters within the YSL form by phase separation.

Since the C-terminus of ZO-1b also harbors an actin binding region (ABR) (Figure 5A) and non-junctional ZO-1b appears to partially co-localize with the cortical actomyosin network within the YSL (Figure S5A-A'), we further hypothesized that the failure of ZO-1bΔC in undergoing phase separation and form non-junctional clusters within the YSL might also be caused by its inability to directly bind actin. To test this possibility, we generated a version of ZO-1b specifically lacking its ABR (ZO-1bΔABR) and substituted full-length ZO-1b with ZO-1bΔABR by expressing ZO-1bΔABR in MZ*zo1b/3* mutant embryos. Unexpectedly, we found that in ZO-1bΔABR expressing MZ*zo1b/3* mutant embryos, non-junctional clusters still formed and underwent fusion similar to the situation when expressing full-length ZO-1b (Figure 5C-C''). However, analysis of cluster size and shape in ZO-1bΔABR expressing

embryos revealed that these clusters were slightly smaller and took more spherical droplet-like shapes than observed when expressing full-length ZO-1b (Figure 5C'''-C''''). This suggests that direct binding of ZO-1b to actin is not required for ZO-1b to undergo phase separation and to form non-junctional clusters within the YSL. Rather, actin binding might restrict the ability of ZO-1b to form larger and more spherical droplet-like clusters within the YSL. Yet, ZO-1b might associate to the actin cytoskeleton indirectly through other domains than its ABR (Hartsock and Nelson, 2008), and thus using the ZO-1bΔABR version might only partially interfere with the ability of ZO-1b to interact with actin. To completely abolish the interaction between non-junctional ZO-1b and actin, we therefore disassembled the actomyosin network within the YSL by exposing embryos to Latrunculin B blocking actin polymerization. Strikingly, disassembly of the actomyosin network within the YSL led to the formation of much larger and more spherical droplet-like clusters of non-junctional ZO-1b within the YSL than found in DMSO-exposed control embryos (Figure 5D-D''). Moreover, these clusters underwent fusion within the YSL despite the notable absence of actomyosin network structures between those clusters (Figures 5E and S5B-B', Movie x), suggesting that these clusters can fuse independently from actomyosin network contraction. Collectively, these findings indicate that ZO-1b forms non-junctional clusters within the YSL by phase separation, and that ZO-1 binding to actin modulates both the size and shape of those clusters.

TJ mechanosensitivity is mediated by retrograde actomyosin flows within the YSL transporting non-junctional phase separated ZO-1b clusters towards the junction

Next, we investigated whether phase separation of ZO-1b and its transport by retrograde actomyosin flows within the YSL towards the TJ at the EVL-YSL boundary confer mechanosensitivity to TJ. To determine whether ZO-1b phase separation is required for TJ mechanosensitivity, we substituted full-length ZO-1b with ZO-1bΔC, incapable of forming phase separated non-junctional clusters within the YSL (Figure 5B), by expressing ZO-1bΔC in MZ*zo-1b/3* mutant embryos. For monitoring TJ mechanosensitivity, we increased YSL actomyosin tension by expressing caRhoA specifically within the YSL and analyzed how this affects junctional accumulation of ZO-1bΔC. We found that junctional ZO-1bΔC levels remained unchanged in response to caRhoA-mediated increased actomyosin tension and flow within the YSL (Figure 6A-A',B-B'), suggesting that the ability to form non-junctional phase separated clusters within the YSL is critical for TJ mechanosensitivity. The failure of ZO-1bΔC to respond to increased actomyosin tension within the YSL is unlikely to be due to

ZO-1bΔC being degraded or non-functional, as the total expression level of these two ZO-1 versions were comparable (Figure S6A-A').

To further determine whether ZO-1b directly binding to Actin is needed for TJ mechanosensitivity, we substituted full-length ZO-1b with ZO-1bΔABR, lacking its actin binding region within the C-terminus, by expressing ZO-1bΔABR in MZ*zo1b/3* mutant embryos. Interestingly, we found that non-junctional ZO-1bΔABR clusters displayed retrograde flow within the YSL similar to clusters formed by full-length ZO-1b (Figure S5C-C'), suggesting that direct binding of ZO-1b to actin is not required for it undergoing actomyosin-contraction dependent retrograde flow within the YSL. However, accumulation of non-junctional ZO-1bΔABR clusters close to the EVL-YSL boundary (Figure S5D-E) and stable incorporation of ZO-1bΔABR clusters into TJ at this boundary were severely reduced with retrogradely flowing ZO-1bΔABR clusters - instead of being incorporated into TJ once arriving at the EVL-YSL boundary (Figure S6B) - frequently 'bypassing' this boundary or detaching from the junctional pool (Figure S6C-C''). Analysis of the subcellular distribution of ZO-1bΔABR clusters within the YSL further revealed that these clusters were not confined to the surface of the YSL, where the actomyosin cortex is located and most of the full-length ZO-1b clusters were found (Figure S6C-C''), but more broadly distributed throughout the YSL (Figure S6C''). This led to some of the ZO-1bΔABR clusters flowing below the TJ complex at the EVL-YSL boundary thereby bypassing this boundary and not being stably incorporated into the TJ. To test whether this reduced junctional incorporation of ZO-1bΔABR interferes with TJ mechanosensitivity, we increased YSL actomyosin tension by expressing caRhoA and analyzed how this affects junctional accumulation of ZO-1bΔABR. Interestingly, we found that the increase in junctional levels of ZO-1bΔABR in response to increased actomyosin tension and flow within the YSL was much less pronounced than observed for full-length ZO-1b (Figure 6C-C'). This suggests that direct binding of ZO-1b to the actomyosin cortex confines non-junctional ZO-1b clusters to the YSL surface where retrograde flows of the actomyosin cortex can effectively transport those clusters towards the TJ to be eventually incorporated there. It, however, also suggests that retrograde flow of non-junctional ZO-1b clusters within the YSL does not require direct binding of ZO-1b to actin, pointing at the possibility that those clusters are transported within the YSL by advection rather than direct interaction with the actomyosin network.

Importantly, while substituting full-length ZO-1b with either ZO-1bΔC or ZO-1bΔABR abolished the effect of increased actomyosin tension on junctional accumulation of ZO-1b, both ZO-1bΔC and ZO-1bΔABR still showed a substantial base-level junctional accumulation at the EVL-YSL boundary. This suggests that retrograde flow and junctional incorporation of ZO-1b clusters within are needed to tune the amount of junctional ZO-1b at EVL-YSL boundary with the tension of the associated YSL actomyosin cytoskeleton, but not for the general accumulation of junctional ZO-1b at this boundary.

TJ mechanosensitivity is required for EVL spreading

Finally, we tested whether TJ mechanosensitivity is required for normal EVL epiboly movements. To this end, we tried to rescue the epiboly phenotype of zo-1b/3 YSL-morphant embryos by injecting mRNA for either the full-length and thus mechanosensitive ZO-1b or the mechano-insensitive ZO-1bΔC and ZO-1bΔABR versions. Specifically, we knocked down ZO-1b and ZO-3 within the YSL by injecting the corresponding MOs into the YSL, and then attempted to rescue the resultant epiboly phenotype by co-injecting a combination of mRNAs encoding ZO-3 together with either full-length ZO-1b (mechanosensitive control) or ZO-1bΔC/ZO-1bΔABR (mechano-insensitive versions of ZO-1b). Strikingly, we found that while the full-length version of ZO-1b in combination with ZO-3 could partially rescue the delay in epiboly progression and actomyosin ring formation in the morphant (Figures 6D-E,D'-E' and 2C-C', Movie 11), expression of ZO-1bΔC or ZO-1bΔABR together with ZO-3 at the same stoichiometric ratios as their full-length counterpart failed to rescue these phenotypes (Figure 6D-E,D'-E' and S6D-D', Movie 11). This suggests that the C-terminus and, specifically, the ABR therein, is important for ZO-1b function in EVL-YSL epiboly movement, and - given that these parts of ZO-1b are also required for ZO-1b mechanosensitivity - that ZO-1b mechanosensitivity is important for EVL-YSL epiboly progression.

Discussion

Our study provides direct evidence that TJ mechanosensitivity is achieved by contractility-driven cortical actomyosin flow transporting phase separated non-junctional ZO-1b clusters towards the junction. Recent biochemical evidence from *in vitro* reconstitution and cell culture experiments suggest that ZO proteins, like other members of MAGUK family (Zeng et al., 2016), can undergo phase separation (Beutel et al.). Our data support these observations by showing that ZO-1b can undergo phase separation within the YSL. Importantly, the ability

of ZO1b to undergo phase separation seems to be required to form non-junctional clusters within the YSL, given that versions of ZO-1b that cannot undergo phase separation, such as ZO-1bΔC (Beutel et al.), are incapable of forming those clusters. Whether other TJ proteins also undergo phase separation and/or localize to ZO-1b non-junctional clusters is not yet entirely clear. Our data so far suggest that TJ adhesion receptors, such as Occludins and Claudins, are exclusively localizing to TJ but do not form non-junctional clusters (Figures S6F-G and S1). The TJ protein Cingulin, in contrast, previously shown to link TJ to the actin cytoskeleton (Guillemot and Citi, 2006; Zihni et al., 2016), colocalizes with both junctional and non-junctional ZO-1b (Figure S6E-E'), pointing at the possibility that TJ adaptor proteins, but not adhesion receptors, can form non-junctional phase separated clusters within the YSL.

Our findings also suggest that ZO-1b binding to actin is critical for ZO-1b cluster formation and function. When the ABR of ZO-1b was deleted or the actomyosin network within the YSL disassembled, then ZO-1b formed more spherical droplet-like clusters within the YSL, suggesting that the actin network limits the inherent tendency of phase separated ZO-1b clusters to round up. This is likely due to actin filaments functioning as a substrate on which ZO-1b clusters adhere and spread. Further, actin filaments appear to restrict the maximum size of ZO-1b clusters, consistent with previous studies showing that the mesh size of elastic polymers can tune the phase separation capacity (Style et al., 2018). Besides influencing the shape and size of ZO-1b clusters, binding to actin also appears to be critical for ZO-1b mechanosensation, given that ZO proteins that lack their ABR within the C-terminus, such as ZO-1bΔABR, failed to respond to changes in actomyosin tension. This loss of mechanosensitivity is likely due to ZO-1bΔABR clusters being less effectively incorporated into TJ, an effect presumably caused by ZO-1bΔABR clusters being less confined to the surface of the YSL, where the actomyosin cortex is located and where those clusters can be most effectively transported towards the TJ at the EVL-YSL boundary. Notably, our observation that the retrograde flow of ZO-1bΔABR clusters within the YSL was largely unaffected suggests that ZO-1 binding to actin is predominantly required for localizing non-junctional ZO-1 clusters to the YSL surface and not transporting it towards the the EVL-YSL boundary. How the retrograde flow of non-junctional ZO-1 clusters within the YSL is achieved is not yet entirely clear, but it is conceivable that advection of the YSL cytoplasm caused by the flow of the actomyosin network might be involved.

TJ mechanosensitivity is likely to be important for both junctional signaling and mechanics at the EVL-YSL boundary. Foremost, it might be required for triggering the formation and maturation of the contractile actomyosin band within the YSL by establishing a positive feedback loop, where actomyosin flow promotes TJ formation (Zihni and Terry, 2015), and TJ promote actomyosin contractility and flow. Our observation that TJ and actomyosin ring formation at the EVL-YSL boundary are interdependent processes, clearly supports this notion. Interestingly, we have only detected retrograde actomyosin and TJ protein flows towards the EVL-YSL junction on the side of the YSL, but not at the leading edge of EVL forming the other side of the contact. While this might be due to technical limitations in imaging such flows in EVL cells that are much smaller than the yolk cell, it is also conceivable that TJ mechanosensitivity is restricted to the side of the YSL. How such potential asymmetric mechanosensitive regulation of TJ at the EVL-YSL boundary affects the biochemical and mechanical function of this junction is not yet clear, but binding of adhesion receptors over the contact might trigger non-autonomous effects eventually equilibrating the amount of TJ components on both sides of the EVL-YSL boundary.

TJ mechanosensitivity might also be required for TJ mechanically linking the EVL margin to the YSL by balancing the coupling strength of TJ to the mechanical force applied to this junction by the contractile actomyosin network within the YSL. Such function has been demonstrated for AJ where junctional tension leads to conformational changes of α-catenin and vinculin, which again increases the Actin-binding capability of these AJ components to the adjacent actomyosin cortex (Gomez et al., 2011). While the role of TJ in regulating cell-cell coupling strength remains largely unknown, recent studies showing that the TJ component ZO-1 modulates tension at cell-cell junctions (Tornavaca et al., 2015); (Hatte et al., 2018) and can be stretched by tension (Spadaro et al., 2017), suggest that ZO proteins are involved in force transduction and reception at cell-cell contacts. Our observation that TJ appear to be the predominant junction type at the EVL-YSL boundary, and that there is force transduction from the actomyosin band within the YSL to the leading edge of the EVL (Behrndt et al., 2012) point at the possibility that TJ have a force-transducing function. Whether and how forces are being transmitted by TJ, and how mechanosensitive junction growth affect such potential function remains to be investigated.

Interestingly, previous studies have suggested that the C-terminus of ZO-1 can fold back on its N-terminal part in an auto-inhibitory fashion, and that this auto-inhibition can be released

by ZO-1 binding to and being stretched by the contractile actomyosin network, thereby allowing it to bind to other junctional proteins (Spadaro et al., 2017). This might explain why versions of ZO-1b lacking either their ABR or entire C-terminus are unable to rescue the epiboly phenotype of MZ*zo1b/3* mutant embryos: their failure to directly bind to the actin cytoskeleton might not only diminishes their localization to the YSL surface and thus their effective incorporation into TJ at the EVL-YSL boundary, but might also interfere with tension-induced conformational changes of ZO-1b required for its biological activity. Future experiments aimed at a systematic structure-function analysis of different ZO proteins will be needed to determine which regions, in addition to the ABR within the C-terminus, binding directly or indirectly to the actin cytoskeleton, are needed to confer mechanosensitivity to those proteins. It will also be interesting to investigate how phase separation at the membrane is initiated - whether clusters form spontaneously through random fluctuations or through pre-existing structures leading to heterogeneous nucleation events (Hyman et al., 2014), or whether there is any additional fine-tuning of critical concentration levels or phase separation capacity via post-translational modifications (Alberti, 2017; Monahan et al., 2017) of ZO proteins.

There is increasing evidence for mechanochemical feedback loops forming the basis of various developmental processes (Goehring and Grill, 2013). A key feature of those feedback loops is the interdependency of mechanical and chemical signals, the concerted action of which drive key cellular processes, such as cell polarization and migration. While the biochemical basis of force-generation and transmission is increasingly well understood (Lecuit et al., 2011), comparable little is yet known about how mechanical forces feed back on biochemical processes. Our findings of mechanical forces promoting the growth of TJ through the generation of actomyosin flow not only unravels that TJ, similar to AJ, are mechanosensitive, but also more broadly points at a yet unrecognized role of TJ in controlling tissue mechanics within the developing organism.

Acknowledgements

References

Alberti, S. (2017). Phase separation in biology. Curr. Biol. *27*, R1097–R1102.

Arboleda-Estudillo, Y., Krieg, M., Stühmer, J., Licata, N.A., Muller, D.J., and Heisenberg, C.-P. (2010). Movement directionality in collective migration of germ layer progenitors. Curr. Biol. *20*, 161–169.

Banani, S.F., Lee, H.O., Hyman, A.A., and Rosen, M.K. (2017). Biomolecular condensates: organizers of cellular biochemistry. Nat. Rev. Mol. Cell Biol. *18*, 285–298.

Bauer, H., Zweimueller-Mayer, J., Steinbacher, P., Lametschwandtner, A., and Bauer, H.C. (2010). The dual role of zonula occludens (ZO) proteins. Biomed Res. Int. *2010*.

Baum, B., and Georgiou, M. (2011). Dynamics of adherens junctions in epithelial establishment, maintenance, and remodeling. J. Cell Biol. *192*, 907–917.

Behrndt, M., Salbreux, G., Campinho, P., Hauschild, R., Oswald, F., Roensch, J., Grill, S.W., and Heisenberg, C.-P. (2012). Forces driving epithelial spreading in zebrafish gastrulation. Science *338*, 257–260.

Benais-Pont, G., Punn, A., Flores-Maldonado, C., Eckert, J., Raposo, G., Fleming, T.P., Cereijido, M., Balda, M.S., and Matter, K. (2003). Identification of a tight junction–associated guanine nucleotide exchange factor that activates Rho and regulates paracellular permeability. J. Cell Biol. *160*, 729–740.

Beutel, O., Maraspini, R., Pombo-Garcia, K., Martin-Lemaitre, C., and Honigmann, A. Phase separation of zonula occludens proteins drives formation of tight junctions.

Bolte, S., and Cordelières, F.P. (2006). A guided tour into subcellular colocalization analysis in light microscopy. J. Microsc. *224*, 213–232.

Brangwynne, C.P., Eckmann, C.R., Courson, D.S., Rybarska, A., Hoege, C., Gharakhani, J., Jülicher, F., and Hyman, A.A. (2009). Germline P granules are liquid droplets that localize by controlled dissolution/condensation. Science *324*, 1729–1732.

Cavey, M., and Lecuit, T. (2009). Molecular bases of cell–cell junctions stability and dynamics. Cold Spring Harbor Perspectives in.

Cavey, M., Rauzi, M., Lenne, P.-F., and Lecuit, T. (2008). A two-tiered mechanism for stabilization and immobilization of E-cadherin. Nature *453*, 751–756.

Cheng, J.C., Miller, A.L., and Webb, S.E. (2004). Organization and function of microfilaments during late epiboly in zebrafish embryos. Dev. Dyn. *231*, 313–323.

Compagnon, J., Barone, V., Rajshekar, S., Kottmeier, R., Pranjic-Ferscha, K., Behrndt, M., and Heisenberg, C.-P. (2014). The notochord breaks bilateral symmetry by controlling cell shapes in the zebrafish laterality organ. Dev. Cell *31*, 774–783.

Cooper, M.S., Szeto, D.P., Sommers-Herivel, G., Topczewski, J., Solnica-Krezel, L., Kang, H.-C., Johnson, I., and Kimelman, D. (2005). Visualizing morphogenesis in transgenic zebrafish embryos using BODIPY TR methyl ester dye as a vital counterstain for GFP. Dev. Dyn. *232*, 359–368.

Cunningham, K.E., and Turner, J.R. (2012). Myosin light chain kinase: pulling the strings of epithelial tight junction function. Ann. N. Y. Acad. Sci. *1258*, 34–42.

Engl, W., Arasi, B., Yap, L.L., Thiery, J.P., and Viasnoff, V. (2014). Actin dynamics modulate mechanosensitive immobilization of E-cadherin at adherens junctions. Nat. Cell Biol. *16*, 587–594.

Fanning, A.S., and Anderson, J.M. (2009). Zonula occludens-1 and-2 are cytosolic scaffolds that regulate the assembly of cellular junctions. Ann. N. Y. Acad. Sci. *1165*, 113–120.

Fanning, A.S., Jameson, B.J., Jesaitis, L.A., and Anderson, J.M. (1998). The tight junction protein ZO-1 establishes a link between the transmembrane protein occludin and the actin cytoskeleton. J. Biol. Chem. *273*, 29745–29753.

Fanning, A.S., Little, B.P., Rahner, C., Utepbergenov, D., Walther, Z., and Anderson, J.M. (2007). The unique-5 and -6 motifs of ZO-1 regulate tight junction strand localization and scaffolding properties. Mol. Biol. Cell *18*, 721–731.

Franke, W.W. (2009). Discovering the molecular components of intercellular junctions—a historical view. Cold Spring Harb. Perspect. Biol.

Gagnon, J.A., Valen, E., Thyme, S.B., Huang, P., Akhmetova, L., Pauli, A., Montague, T.G., Zimmerman, S., Richter, C., and Schier, A.F. (2014). Efficient mutagenesis by Cas9 protein-mediated oligonucleotide insertion and large-scale assessment of single-guide RNAs. PLoS One *9*, e98186.

Godsel, L.M., Getsios, S., Huen, A.C., and Green, K.J. (2004). The molecular composition and function of desmosomes. Handb. Exp. Pharmacol. 137–193.

Goehring, N.W., and Grill, S.W. (2013). Cell polarity: mechanochemical patterning. Trends Cell Biol. *23*, 72–80.

Gomez, G.A., McLachlan, R.W., and Yap, A.S. (2011). Productive tension: force-sensing and homeostasis of cell–cell junctions. Trends Cell Biol. *21*, 499–505.

Guillemot, L., and Citi, S. (2006). Cingulin, a Cytoskeleton-Associated Protein of the Tight Junction. In Tight Junctions, L. Gonzalez-Mariscal, ed. (Boston, MA: Springer US), pp. 54–63.

Hartsock, A., and Nelson, W.J. (2008). Adherens and tight junctions: structure, function and connections to the actin cytoskeleton. Biochim. Biophys. Acta *1778*, 660–669.

Hatte, G., Prigent, C., and Tassan, J.-P. (2018). Tight junctions negatively regulate mechanical forces applied to adherens junctions in vertebrate epithelial tissue. J. Cell Sci. *131*.

Holloway, B.A., de la Torre Canny, S.G., Ye, Y., Slusarski, D.C., Freisinger, C.M., Dosch, R., Chou, M.M., Wagner, D.S., and Mullins, M.C. (2009). A Novel Role for MAPKAPK2 in Morphogenesis during Zebrafish Development. PLoS Genet. *5*, e1000413.

Hyman, A.A., Weber, C.A., and Jülicher, F. (2014). Liquid-liquid phase separation in biology. Annu. Rev. Cell Dev. Biol. *30*, 39–58.

Iioka, H., Ueno, N., and Kinoshita, N. (2004). Essential role of MARCKS in cortical actin dynamics during gastrulation movements. J. Cell Biol. *164*, 169–174.

Itoh, M., Tsukita, S., Yamazaki, Y., and Sugimoto, H. (2012). Rho GTP exchange factor ARHGEF11 regulates the integrity of epithelial junctions by connecting ZO-1 and RhoA-myosin II signaling. Proc. Natl. Acad. Sci. U. S. A. *109*, 9905–9910.

Jayashankar, V., Nguyen, M.J., Carr, B.W., and Zheng, D.C. (2013). Protein phosphatase 1 β paralogs encode the zebrafish myosin phosphatase catalytic subunit. PLoS One.

Johnson, J.L., Najor, N.A., and Green, K.J. (2014). Desmosomes: regulators of cellular signaling and adhesion in epidermal health and disease. Cold Spring Harb. Perspect. Med. *4*, a015297.

Kato, M., Han, T.W., Xie, S., Shi, K., Du, X., Wu, L.C., Mirzaei, H., Goldsmith, E.J., Longgood, J., Pei, J., et al. (2012). Cell-free formation of RNA granules: low complexity sequence domains form dynamic fibers within hydrogels. Cell *149*, 753–767.

Keller, P.J., Schmidt, A.D., Wittbrodt, J., and Stelzer, E.H.K. (2008). Reconstruction of zebrafish early embryonic development by scanned light sheet microscopy. Science *322*, 1065–1069.

Kimmel, R.A., and Meyer, D. (2010). Molecular regulation of pancreas development in zebrafish. Methods Cell Biol. *100*, 261–280.

Kimmel, C.B., Ballard, W.W., Kimmel, S.R., Ullmann, B., and Schilling, T.F. (1995). Stages of embryonic development of the zebrafish. Dev. Dyn. *203*, 253–310.

Köppen, M., Fernández, B.G., Carvalho, L., Jacinto, A., and Heisenberg, C.-P. (2006). Coordinated cell-shape changes control epithelial movement in zebrafish and Drosophila. Development *133*, 2671–2681.

Kwan, K.M., Fujimoto, E., and Grabher, C. (2007). The Tol2kit: A multisite gateway-based construction kit for Tol2 transposon transgenesis constructs. Dynamics: An Official ….

Labun, K., Montague, T.G., Gagnon, J.A., Thyme, S.B., and Valen, E. (2016). CHOPCHOP v2: a web tool for the next generation of CRISPR genome engineering. Nucleic Acids Res. *44*, W272–W276.

Ladoux, B., Anon, E., Lambert, M., Rabodzey, A., Hersen, P., Buguin, A., Silberzan, P., and Mège, R.-M. (2010). Strength dependence of cadherin-mediated adhesions. Biophys. J. *98*, 534–542.

Lecuit, T., Lenne, P.-F., and Munro, E. (2011). Force generation, transmission, and integration during cell and tissue morphogenesis. Annu. Rev. Cell Dev. Biol. *27*, 157–184.

Li, P., Banjade, S., Cheng, H.-C., Kim, S., Chen, B., Guo, L., Llaguno, M., Hollingsworth, J.V., King, D.S., Banani, S.F., et al. (2012). Phase transitions in the assembly of multivalent signalling proteins. Nature *483*, 336–340.

Li, Q., Lau, A., Morris, T.J., Guo, L., Fordyce, C.B., and Stanley, E.F. (2004). A Syntaxin 1, Gαo, and N-Type Calcium Channel Complex at a Presynaptic Nerve Terminal: Analysis by Quantitative Immunocolocalization. J. Neurosci. *24*, 4070–4081.

Lye, M.F., Fanning, A.S., Su, Y., Anderson, J.M., and Lavie, A. (2010). Insights into regulated ligand binding sites from the structure of ZO-1 Src homology 3-guanylate kinase module. J. Biol. Chem. *285*, 13907–13917.

Maître, J.-L., Berthoumieux, H., Krens, S.F.G., Salbreux, G., Jülicher, F., Paluch, E., and Heisenberg, C.-P. (2012). Adhesion functions in cell sorting by mechanically coupling the cortices of adhering cells. Science *338*, 253–256.

Matter, K., and Balda, M.S. (2003). Signalling to and from tight junctions. Nat. Rev. Mol. Cell Biol. *4*, 225–236.

Meeker, N.D., Hutchinson, S.A., Ho, L., and Trede, N.S. (2007). Method for isolation of PCR-ready genomic DNA from zebrafish tissues. Biotechniques *43*, 610, 612, 614.

Miesfeld, J.B., Gestri, G., Clark, B.S., Flinn, M.A., Poole, R.J., Bader, J.R., Besharse, J.C., Wilson, S.W., and Link, B.A. (2015). Yap and Taz regulate retinal pigment epithelial cell fate. Development *142*, 3021–3032.

Monahan, Z., Ryan, V.H., Janke, A.M., Burke, K.A., Rhoads, S.N., Zerze, G.H., O'Meally, R., Dignon, G.L., Conicella, A.E., Zheng, W., et al. (2017). Phosphorylation of the FUS low-complexity domain disrupts phase separation, aggregation, and toxicity. EMBO J. *36*, 2951–2967.

Montague, T.G., Cruz, J.M., Gagnon, J.A., Church, G.M., and Valen, E. (2014). CHOPCHOP: a CRISPR/Cas9 and TALEN web tool for genome editing. Nucleic Acids Res. *42*, W401–W407.

Nekrasova, O., and Green, K.J. (2013). Desmosome assembly and dynamics. Trends Cell Biol. *23*, 537–546.

Niessen, C.M. (2007). Tight junctions/adherens junctions: basic structure and function. J. Invest. Dermatol. *127*, 2525–2532.

Otani, T., Ichii, T., Aono, S., and Takeichi, M. (2006). Cdc42 GEF Tuba regulates the junctional configuration of simple epithelial cells. J. Cell Biol. *175*, 135–146.

Preibisch, S., Saalfeld, S., and Tomancak, P. (2009). Globally optimal stitching of tiled 3D microscopic image acquisitions. Bioinformatics *25*, 1463–1465.

Shaner, N.C., Lambert, G.G., Chammas, A., Ni, Y., Cranfill, P.J., Baird, M.A., Sell, B.R., Allen, J.R., Day, R.N., Israelsson, M., et al. (2013). A bright monomeric green fluorescent protein derived from Branchiostoma lanceolatum. Nat. Methods *10*, 407–409.

Shen, L., Weber, C.R., and Turner, J.R. (2008). The tight junction protein complex undergoes rapid and continuous molecular remodeling at steady state. J. Cell Biol. *181*, 683–695.

Shin, K., Fogg, V.C., and Margolis, B. (2006). Tight junctions and cell polarity. Annu. Rev. Cell Dev. Biol. *22*, 207–235.

Smutny, M., Ákos, Z., Grigolon, S., Shamipour, S., Ruprecht, V., Čapek, D., Behrndt, M., Papusheva, E., Tada, M., Hof, B., et al. (2017). Friction forces position the neural anlage. Nat. Cell Biol. *19*, 306–317.

Sommer, C., Straehle, C., Köthe, U., and Hamprecht, F.A. (2011). Ilastik: Interactive learning and segmentation toolkit. In 2011 IEEE International Symposium on Biomedical Imaging: From Nano to Macro, pp. 230–233.

Spadaro, D., Le, S., Laroche, T., Mean, I., Jond, L., Yan, J., and Citi, S. (2017). Tension-Dependent Stretching Activates ZO-1 to Control the Junctional Localization of Its Interactors. Curr. Biol. *27*, 3783–3795.e8.

Style, R.W., Sai, T., Fanelli, N., Ijavi, M., Smith-Mannschott, K., Xu, Q., Wilen, L.A., and Dufresne, E.R. (2018). Liquid-Liquid Phase Separation in an Elastic Network. Phys. Rev. X *8*, 011028.

Takesono, A., Moger, J., Farooq, S., Cartwright, E., Dawid, I.B., Wilson, S.W., and Kudoh, T. (2012). Solute carrier family 3 member 2 (Slc3a2) controls yolk syncytial layer (YSL) formation by regulating microtubule networks in the zebrafish embryo. Proc. Natl. Acad. Sci. U. S. A. *109*, 3371–3376.

Talbot, J.C., and Amacher, S.L. (2014). A streamlined CRISPR pipeline to reliably generate zebrafish frameshifting alleles. Zebrafish *11*, 583–585.

Tornavaca, O., Chia, M., Dufton, N., and Almagro, L.O. (2015). ZO-1 controls endothelial adherens junctions, cell–cell tension, angiogenesis, and barrier formation. J. Cell Biol.

Utepbergenov, D.I., Fanning, A.S., and Anderson, J.M. (2006). Dimerization of the scaffolding protein ZO-1 through the second PDZ domain. J. Biol. Chem. *281*, 24671–24677.

Van Itallie, C.M., and Anderson, J.M. (2014). Architecture of tight junctions and principles of molecular composition. Semin. Cell Dev. Biol. *36*, 157–165.

Villefranc, J.A., Amigo, J., and Lawson, N.D. (2007). Gateway compatible vectors for analysis of gene function in the zebrafish. Dev. Dyn. *236*, 3077–3087.

Westerfield, M. (2007). The zebrafish book: a guide for the laboratory use of zebrafish (Danio rerio) (University of Oregon press).

Wheelock, M.J., and Johnson, K.R. (2003). Cadherin-mediated cellular signaling. Curr. Opin. Cell Biol. *15*, 509–514.

Wittchen, E.S., Haskins, J., and Stevenson, B.R. (2003). NZO-3 expression causes global changes to actin cytoskeleton in Madin-Darby canine kidney cells: linking a tight junction protein to Rho GTPases. Mol. Biol. Cell *14*, 1757–1768.

Ye, F., Zeng, M., and Zhang, M. (2018). Mechanisms of MAGUK-mediated cellular junctional complex organization. Curr. Opin. Struct. Biol. *48*, 6–15.

Zeng, M., Shang, Y., Araki, Y., Guo, T., Huganir, R.L., and Zhang, M. (2016). Phase Transition in Postsynaptic Densities Underlies Formation of Synaptic Complexes and Synaptic Plasticity. Cell *166*, 1163–1175.e12.

Zihni, C., and Terry, S.J. (2015). RhoGTPase signalling at epithelial tight junctions: Bridging the GAP between polarity and cancer. Int. J. Biochem. Cell Biol. *64*, 120–125.

Zihni, C., Mills, C., Matter, K., and Balda, M.S. (2016). Tight junctions: from simple barriers to multifunctional molecular gates. Nat. Rev. Mol. Cell Biol. *17*, 564–580.
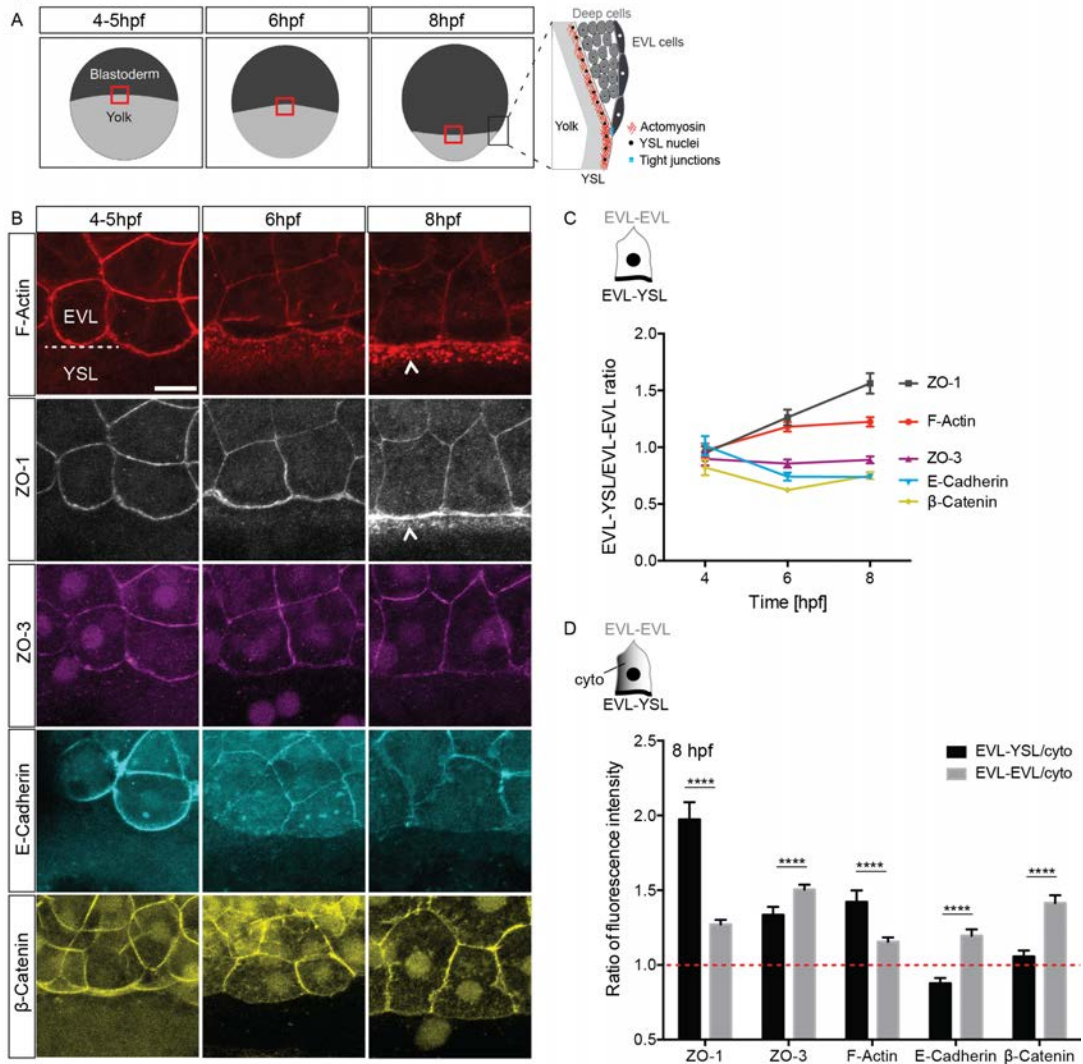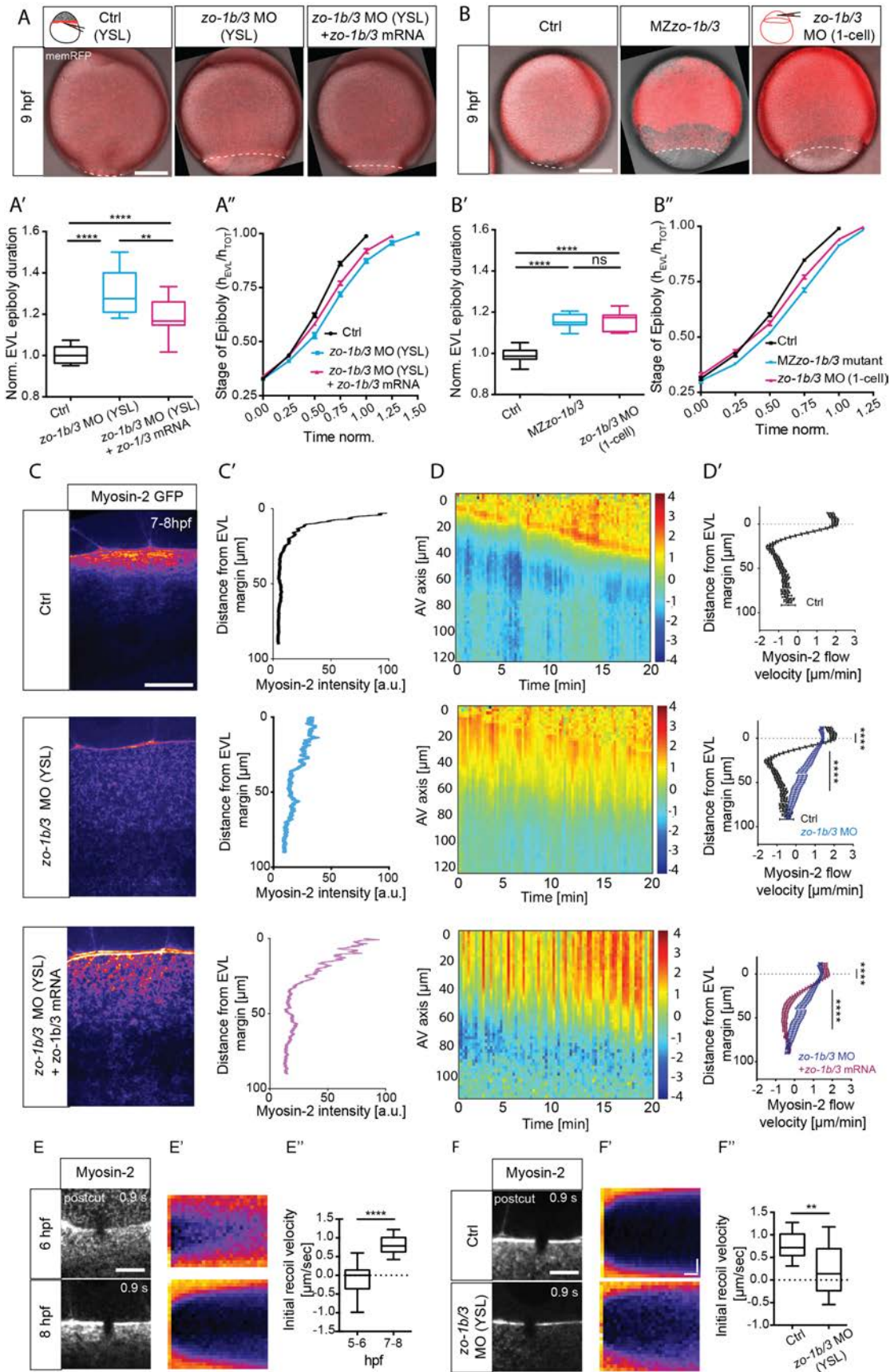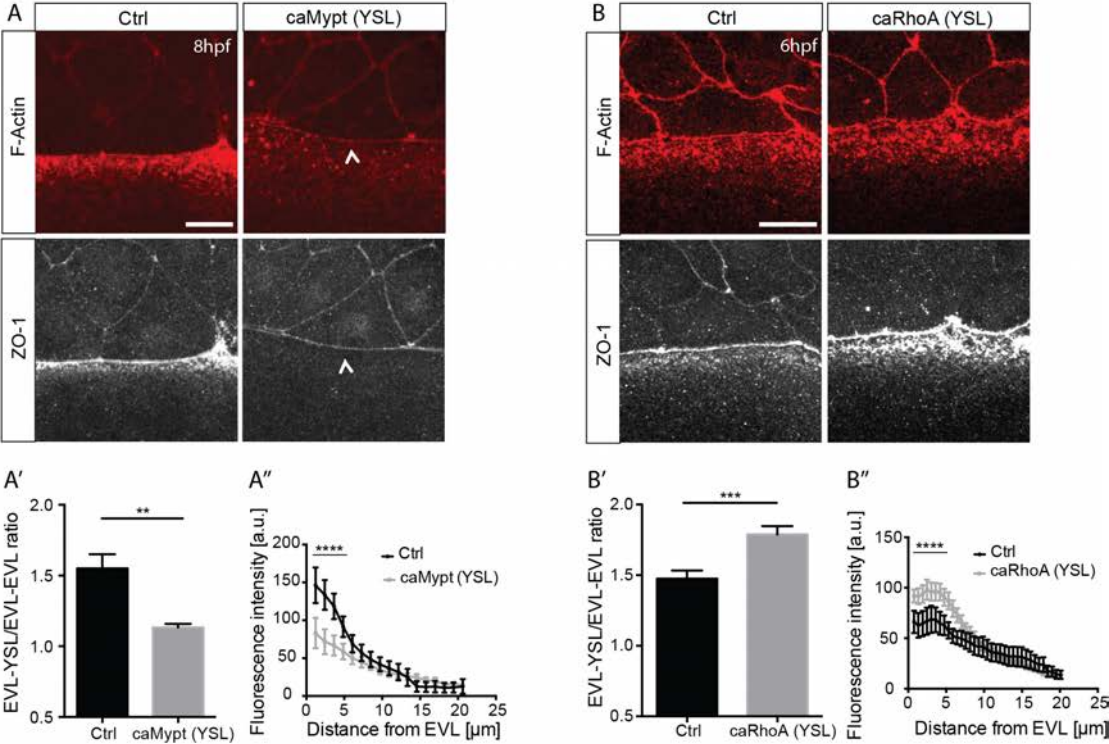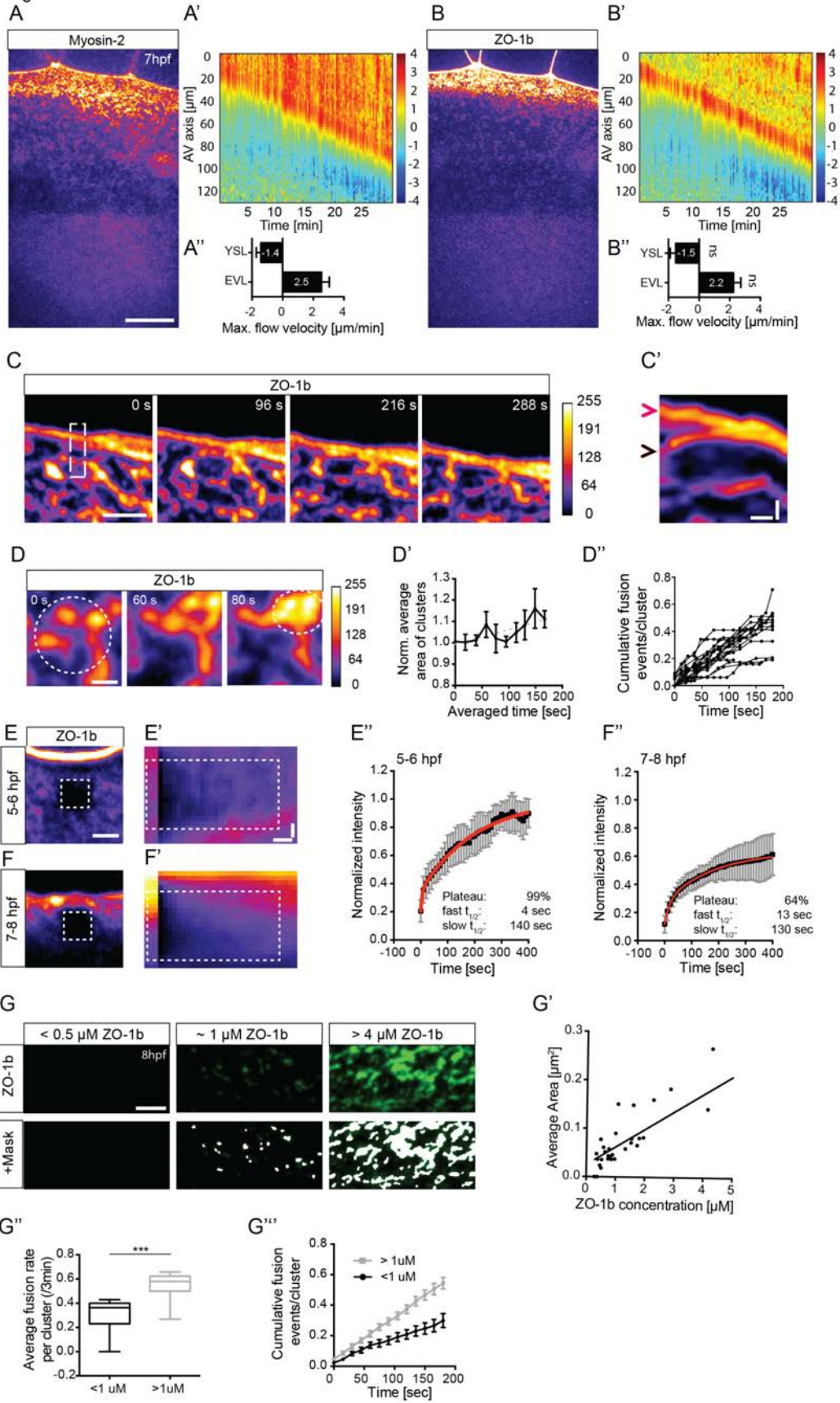
Figure 1

Figure 2

Figure 3

Figure 4

Figure 5

A

ZO-1b full length

ZO-1b ΔC

ZO-1b ΔABR

B | **C**

C' | **C''** | **C'''** | **C''''**

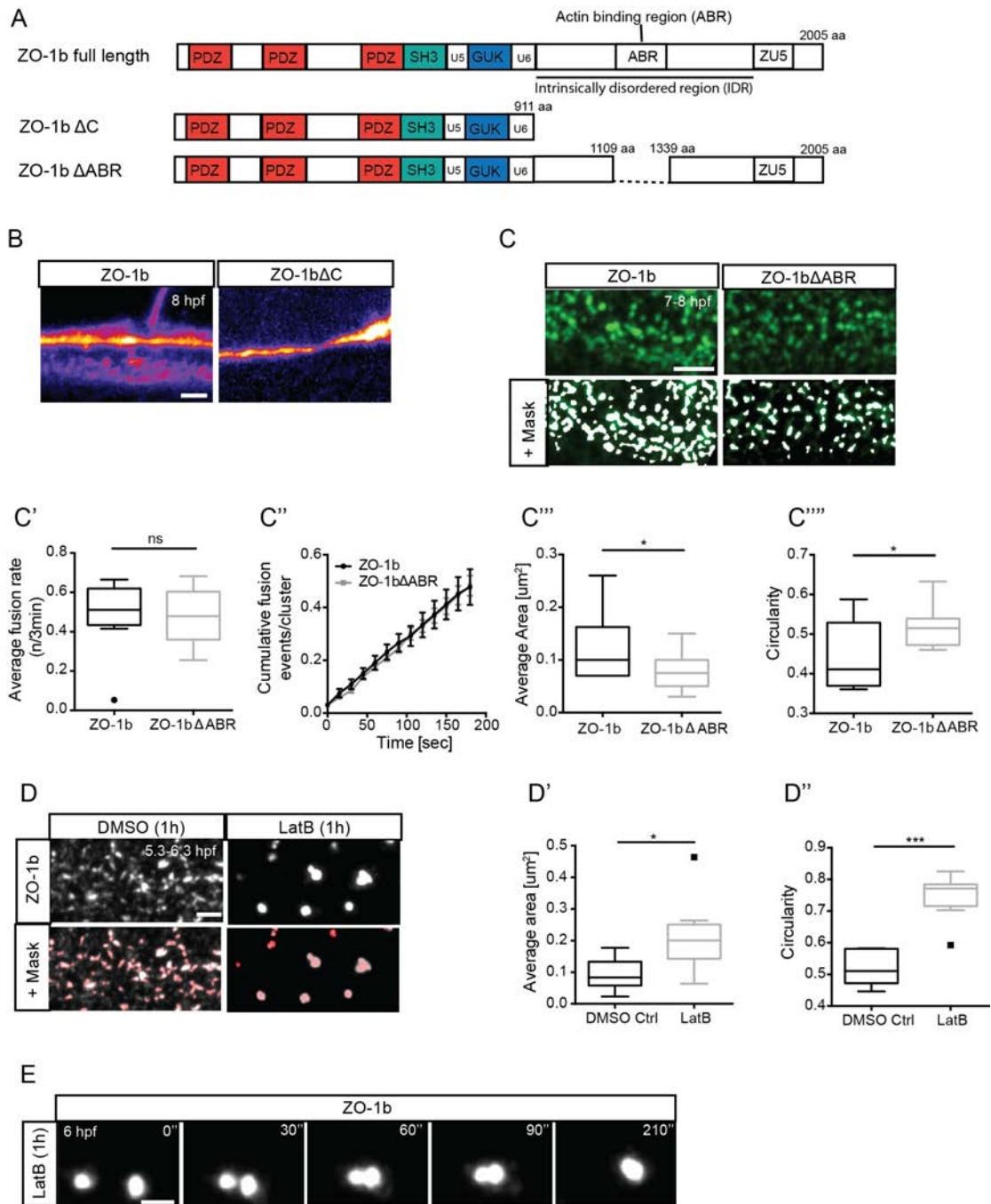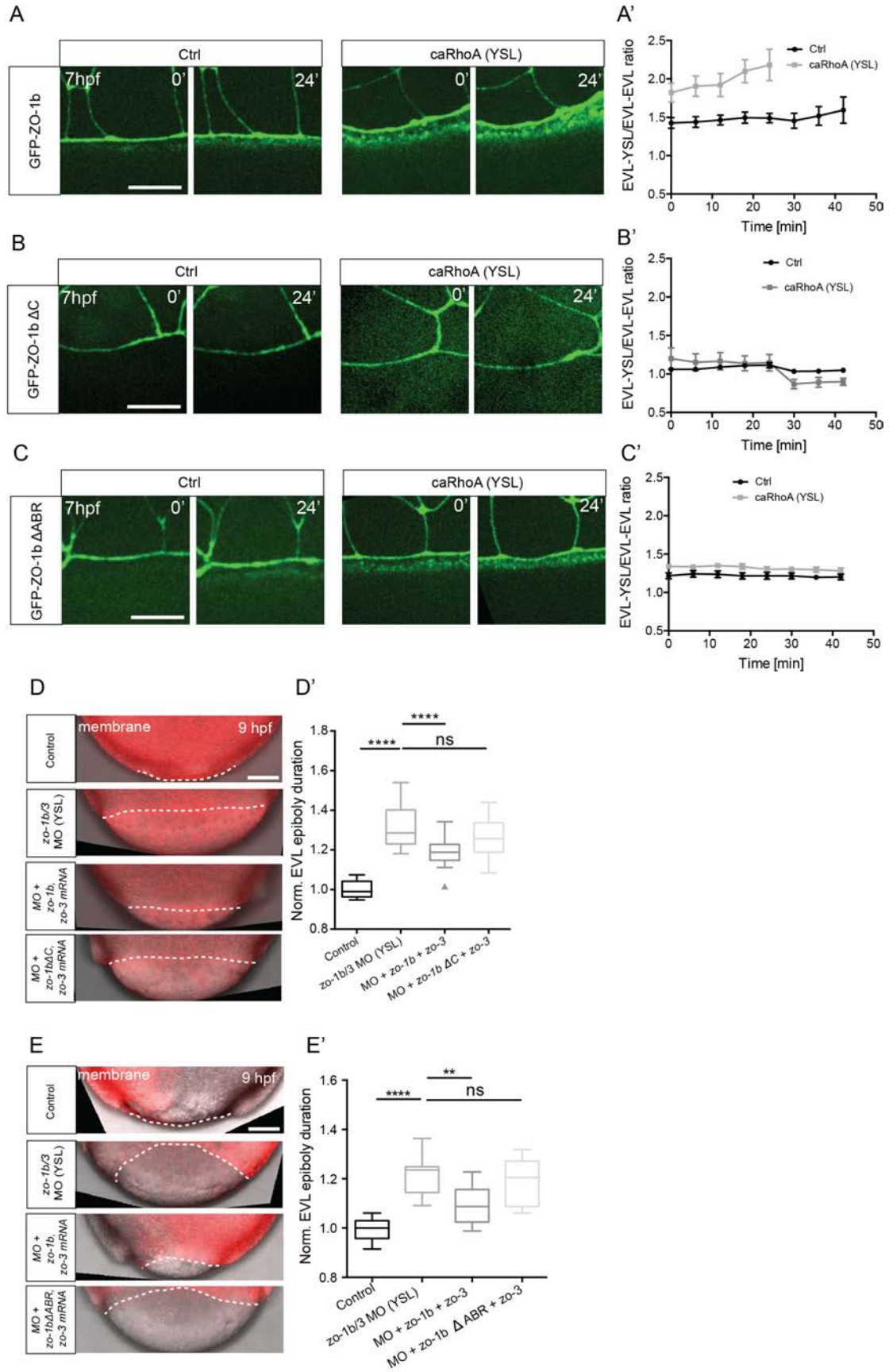**D** | **D'** | **D''**

E

Figure 6

Figure legends

Figure 1. Tight junction components accumulate at the EVL-YSL boundary

(A) Schematic representation of EVL spreading during consecutive stages of epiboly (4-5, 6 and 8 hpf). Yolk cell. light grey; blastoderm (EVL and deep cells), dark grey. Red rectangle demarcates regions of the EVL-YSL boundary shown in (B). Black rectangle demarcates region of enlarged sagittal view outlining the tissue structure at 8 hpf.

(B) Maximum intensity projections (MIPs) of F-actin (Phalloidin, 1st row), ZO-1 (2nd row), ZO-3 (3rd row), E-Cadherin (4th row), and β-Catenin (5th row) localization at the EVL-YSL boundary at 4-5 hpf (left column), 6 hpf (middle column) and 8 hpf (right column). ZO-1, ZO-3 and E-Cadherin were detected by immunohistochemistry. White arrowheads point to increased accumulation at the EVL-YSL boundary. Scale bar, 20 μm.

(C) Plot of EVL-YSL junctional intensity normalized to EVL-EVL junctional intensity as a function of time during EVL epiboly (see also schematic above). Data are mean at 95% confidence. F-actin with N=2 and n=15 cells at 4-5 hpf, n=42 cells at 6 hpf and n=46 cells at 8 hpf. ZO-1 with N=2 and n=15 cells at 4-5 hpf, n=42 cells at 6 hpf and n=46 cells at 8 hpf. ZO-3 with N=2 and n=26 cells at 4-5 hpf, n=52 cells at 6 hpf, n=58 cells at 8 hpf. E-Cadherin with N=3 and n=29 cells at 4-5 hpf, with N=2 and n=32 cells at 6hpf, N=3 and n=84 cells at 8 hpf. β-Catenin with N=2 and n=54 cells at 4-5 hpf, n=29 cells at 6 hpf, n=28 cells at 8 hpf.

(D) Plot of EVL-YSL junctional intensity (black) and EVL-EVL junctional intensity (grey) normalized to cytoplasmic intensity at 8hpf. Red dashed line indicates ratio of 1 demarcating the boundary between accumulation (>1) and depletion (<1). Data are mean at 95% confidence. F-Actin and ZO-1 with N=2 and n=46 cells, ZO-3 with N=2 and n=58 cells. E-Cadherin with N=2 and n=40 cells. β-Catenin with N=2 and n=28 cells. Statistical test for F-Actin, ZO-3 and E-Cadherin, Mann-Whitney test with ****$p < 0.0001$; ZO-1 and β-Catenin, Unpaired t test with ****$p < 0.0001$.

Figure 2. ZO-1b and 3 are required for proper EVL epiboly movements, and actomyosin flows and tension within the YSL

(A,B) Maximum intensity projections (MIPs) of brightfield/fluorescence images of embryos injected directly into the YSL at high stage (3.3 hpf) with phenol red and H2A-mcherry (ctrl, left panel), *zo-1b* MO (1.5 ng) and *zo-3* MO (0.5 ng) (middle panel), and *zo-1b/3* MO together with GFP-tagged *zo-1b* mRNA (25 pg) and GFP-tagged *zo-3* mRNA (mutated for MO recognition site, 5 pg) (right panel) at 9 hpf (A) and wild-type (wt) control embryos (ctrl, left

panel), MZ*zo-1b/3* mutant (middle panel) and morphant embryos (injected with 1.5 ng of *zo-1b* MO and 0.5 ng of *zo-3* MO at 1-cell stage, right panel) at 9 hpf (B). Plasma membrane is marked by membrane-RFP to outline cells. EVL-YSL boundary is marked by white dashed line to demarcate extent of EVL epiboly in the different conditions. Schemes of different injection methods showing injection into the YSL (A) to obtain YSL-specific knock-down and into the 1-cell stage embryo (B) to gain ubiquitous knock-down. Scale bar, 200 µm.

(A', B') Plot of total time required for EVL to complete epiboly for the conditions shown in (A,B) and normalized to average time needed by control embryos. (A') YSL-ctrl in black with N=3, n=11 embryos; YSL-morphant in cyan with N=3, n=12 embryos; and YSL morphant rescue in magenta with N=3, n=11 embryos. (B') wt control in black with N=4, n=11 embryos and 1-cell stage injected controls in black for morphant with N=3, n=11 embryos; mutant in cyan with N=4, n=13 embryos, and morphant in magenta with N=3, n=8 embryos. Data are shown as box-and-whisker plots (Whiskers: Tukey). Ordinary one-way ANOVA with Tukey's multiple comparisons test with ****$p < 0.0001$, ***$p < 0.001$ (A') and one-way ANOVA with Tukey's multiple comparisons test ****$p < 0.0001$ (B').

(A'',B'') Plot of EVL tissue spreading, expressed as height of EVL (h_{EVL}) normalized to total embryo height (h_{TOT}), as a function of time normalized to average time needed by control embryos for the conditions shown in (A,B). N/n as in (A',B'). Data are mean ± s.e.m.

(C) MIPs of Myosin-2 localization at the EVL-YSL boundary in Tg(*actb1:myl12.1-eGFP*) YSL-ctrl (phenol red injected), *zo-1b/3* YSL-morphant (1.5ng, 0.5 ng into the YSL) and *zo-1b/3* YSL-morphant embryos rescued by co-injection of GFP-tagged *zo-1b* (25 pg) and *zo-3* (5 pg, mutated for MO recognition site) mRNAs at 7-8 hpf. Scale bar, 20µm.

(C') Plot of Myosin-2 intensity as a function of distance from EVL margin in an exemplary YSL-ctrl, *zo-1b/3* YSL-morphant and rescued *zo-1b/3* MO YSL-morphant embryos at 7-8 hpf. [a.u.] arbitrary units.

(D) Kymograph of Myosin-2 flow velocities along the animal-vegetal (AV) axis of the embryo as a function of time during epiboly in an exemplary YSL-ctrl, *zo-1b/3* YSL-morphant and *zo-1b/3* rescued YSL-morphant embryo at 7-8 hpf. Kymograph ranges from negative values (in blue) indicating retrograde flows towards the EVL margin to positive values (in red) indicating anterograde flows towards the vegetal pole.

(D') Plot of Myosin-2 mean flow velocities along AV axis averaged over 7.5-30 min in YSL-ctrl, *zo-1b/3* YSL-morphant and rescued *zo-1b/3* YSL-morphant embryos between 7 and 8 hpf. EVL peak velocities averaged over 10 µm, Unpaired t test, ****$p < 0.0001$; YSL peak velocities averaged over 45 µm (15 - 60 µm from EVL margin), Mann-Whitney test , ****$p <$

0.0001. YSL-ctrl with N=4, n=8 embryos and *zo-1b/3* YSL-morphant with N=5, n=8 embryos. Rescued *zo-1b/3* YSL-morphant, N=6, n=13 embryos.

(E,F) MIPs of the EVL-YSL boundary in Myosin-2 expressing Tg(*actb1:myl12.1-eGFP*) wt embryos at 6 and 8 hpf (E), YSL-ctrl and *zo-1b/3* YSL-morphant (F, 1.5 ng of *zo-1b* MO and 0.5ng of *zo-3* MO into the YSL) embryos at 7-8 hpf after (4th post-cut frame) UV laser-cutting along a 5 μm line oriented perpendicular to the boundary. Scale bar, 10μm.

(E',F') Exemplary kymographs of EVL-YSL junctional opening in response to UV-laser cutting as a function of time for the conditions shown in (E,F). Horizontal scale bar, 1.2 s; vertical scale bar, 1 μm.

(E'',F'') Plot of initial recoil velocities of EVL-YSL junction after UV-laser cutting for the conditions shown in (E,F). Data are shown as box-and-whisker plots (whiskers: Tukey). Unpaired t test with ****$p < 0.0001$; **$p = 0.0073$. YSL-ctrl and *zo-1b/3* YSL-morphant with N=2, n=12 cells.

Figure 3. Actomyosin contractility affects ZO-1 recruitment to the EVL-YSL boundary

(A,B) Maximum intensity projections (MIPs) of F-actin (Phalloidin, 1st row) and ZO-1 (2nd row) localization at the EVL-YSL junction in embryos that were either injected into the YSL at high stage (3.3 hpf) with H2A-mcherry mRNA (100pg, left column, ctrl) and caMypt (75pg caMypt plus 25pg H2A-mcherry, right column) shown at 8 hpf (A), or injected into marginal blastomeres/YSL at 128-cell stage with H2B-EGFP (2.3-2.5 pg - left column, ctrl) and caRhoA mRNA (0.3-0.5 pg caRhoA plus 2 pg H2B-GFP, right column) shown at 6 hpf (B). ZO-1 was detected by immunohistochemistry. White arrowheads point to decrease (A) or increase (B) in signal at the EVL-YSL boundary. Scale bar, 20μm.

(A',B') Plot of junctional ZO-1 intensity ratio (EVL-YSL/EVL-EVL) for the conditions described in (A,B). (A) Ctrl with N=2, n=44 cells; caMypt with N=2, n=39 cells. (B) Ctrl with N=2, n=28 cells; caRhoA with N=2, n=52 cells. Data are shown as mean plus s.e.m.; Mann-Whitney test; ** $p = 0.0007$.

(A'',B'') Plot of non-junctional ZO-1 fluorescent intensity as a function of distance from the EVL margin for the conditions shown in (A,B). Data are shown as mean plus s.e.m. Unpaired t test of non-junctional pool within first 5 μm from EVL margin with ****$p < 0.0001$ (A). Mann-Whitney test of non-junctional ZO-1 within first 5 μm from EVL margin with ****$p < 0.0001$ (B). (A) Ctrl with N=2, n=6 embryos; caMypt with N=2,n=7 embryos. (B) Ctrl with N=2, n=6 embryos; caRhoA with N=2, n=9 embryos.

Figure 4. Non-junctional clusters of ZO-1b within the YSL undergo retrograde flows and are incorporated into TJ at the EVL-YSL boundary

(A,B) Maximum intensity projections (MIPs) of Myosin-2 (A) or ZO-1b (B) localization at the EVL-YSL boundary in Tg(*actb1:myl12.1-mcherry*; *actb1:mNEONgreen-zfTjp1b*) embryos at 7-8 hpf. Scale bar, 20μm.

(A',B') Exemplary kymographs of Myosin-2 (A') or ZO-1b (B') flow velocities along the animal-vegetal (AV) axis of the YSL as a function of time during epiboly. Kymograph ranges from negative (retrograde flows towards the EVL-YSL boundary, blue) to positive (anterograde flows away from the EVL-YSL boundary, red) values.

(A'',B'') Maximum Myosin-2 (A") and ZO-1b (B") flow velocities, indicating peak retrograde flow rates within the YSL (negative value) and maximum epiboly movement velocity of the EVL-YSL boundary (positive value). N=4, n=7 embryos. Mann-Whitney test, ns not significant.

(C) Consecutive MIP high-resolution (Airy Scan) images of non-junctional ZO-1b being incorporated at the EVL-YSL boundary in a Tg(*actb1:mNEONgreen-zfTjp1b*) embryo at 7-8 hpf. Horizontal scale bar, 48 s; Vertical scale bar, 2 μm. Calibration bar showing LUT for grey value range.

(C') Kymograph of boxed region in (C) showing non-junctional ZO-1b cluster (black arrowhead) incorporation at the EVL-YSL boundary (pink arrowhead). Horizontal scale bar, 40 s; vertical scale bar, 1 μm.

(D) Consecutive MIP high-resolution (Airy Scan) images of non-junctional ZO-1b clusters undergoing fusion close to the EVL-YSL boundary (within 15 μm distance to EVL) in a Tg(*actb1:mNEONgreen-zfTjp1b*) embryo at 6.5-8 hpf. White dashed circle shows region of fusing non-junctional clusters. Scale bar, 500 nm. Calibration bar showing LUT for grey value range.

(D') Plot of average ZO-1b non-junctional cluster size normalized to initial average size within the YSL as a function of time between 5.7-8 hpf. Cluster size was averaged over acquisition times of 20 s +/- 5.5 s. N=5, n=9 embryos.

(D'') Plot of cumulative fusion events per ZO-1b cluster as a function of time in Tg(*actb1:mNEONgreen-zfTjp1b*) embryos at 6-8 hpf. Each line represents fusion events averaged per embryo. N=5, n=15 embryos.

(E,F) Sum intensity projection image (sum of all slices) of ZO-1b signal in Tg(*actb1:mNEONgreen-zfTjp1b*) embryos within the YSL (2-5 μm from EVL margin) (E with N=4, n=13 embryos and F with N=4, n=12 embryos) after bleaching in FRAP experiments at

early-mid (5-6 hpf; E) and late epiboly stage (7-8 hpf; F). White dashed box outlines bleached region. Scale bar, 5 μm.

(E',F') Exemplary kymograph of bleached region for the conditions described in (E,F). White dashed box outlines region used for intensity measurements. Horizontal scale bar, 40 s; vertical scale bar, 1 μm.

(E'',F'') Plot of GFP-ZO-1b fluorescence recovery as a function of time for the conditions described in (E,F). Data are mean ± SD. Intensity values were normalized to the pre-bleach intensities and to non-junctional signals (E,F) to correct for bleaching (more details see Materials and Methods). Solid line shows a double exponential fit (E'',F'').

(G) MIP high-resolution (Airy Scan) images of non-junctional GFP-ZO-1b clusters within the YSL of MZ*zo-1b/3* mutants injected at 1-cell with different concentrations of *GFP-zo-1b* mRNAs (50 pg - 150 pg mRNA) at 7-8 hpf. 1st row, GFP signal only; 2nd row, GFP signal (green) overlaid with white signal obtained by cluster masking using Ilastik (for details see Materials and Methods). ZO-1b concentrations in μM were determined via quantitative fluorescence microscopy. Calibration curves (see Figure S4C) were acquired with the same imaging settings. Scale bar, 2 μm.

(G') Plot of average area of ZO-1b clusters as a function of ZO-1b concentration. N=3, n=33 embryos.

(G'') Bar plot of average fusion rate per ZO-1b cluster for different ZO-1b concentrations within the YSL. Average fusion rate was determined as the total fusion number divided by the average cluster number in a time window of 3 min. Data are shown as box-and-whisker plots (Whiskers: Tukey). Mann Whitney test. ***p = 0.001. N=3, n=32 embryos.

(G''') Plot of cumulative fusion events per ZO-1b cluster as a function of time. Curves show the different ZO-1b concentrations. Data are shown as mean plus s.e.m. N/n see (G'').

Figure 5. Non-junctional ZO-1b undergoes phase separation within the YSL

(A) Schematic representation of the domain structure of full length ZO-1b, ZO-1b- C construct, lacking its mainly intrinsically disordered C-terminus including an Actin binding region (ABR) and ZO-1b-*Δ*ABR construct, only lacking the ABR within the IDR.

(B) MIP high-resolution (Airy Scan) images of MZ*zo-1b/3* mutant embryos injected at 1-cell stage with either *GFP-zo-1b* (50 pg, control) or *GFP-zo-1bΔC* (30 pg) mRNAs at 8hpf. Scale bar, 2 μm.

(C,D) MIP high-resolution (Airy Scan) images of non-junctional ZO-1b clusters within the YSL of MZ*zo-1b/3* mutants injected at 1-cell stage with either *GFP-zo-1b* (50 pg, control) or *GFP-*

zo-1bΔABR (44 pg) at 7-8 hpf (C). MIP high-resolution (Airy Scan) images of Tg(*actb1:mNEONgreen-zfTjp1b*) embryos treated for 1h with either DMSO (control) or 1 µg/ml Latrunculin B prior to imaging at 5.3-6.3 hpf (D). 1st row, GFP signal only; 2nd row, GFP signal (green) overlaid with white signal obtained by cluster masking using Ilastik (for details see Materials and Methods). Scale bar, 2 µm.

(C') Bar plot of average fusion rate per ZO-1b and ZO-1bΔABR cluster within the YSL. Average fusion rate was determined as the total fusion number divided by the average cluster number in a time window of 3 min. Data are shown as box-and-whisker plots (Whiskers: Tukey); Mann Whitney test; ns. not significant. ZO1b with N=4, n= 8 embryos. ZO-1bΔABR with N=4, n=12 embryos.

(C'') Plot of cumulative fusion events per ZO-1b cluster as a function of time. Curves show the different ZO-1b concentrations. Data are shown as mean plus s.e.m. N/n see (G'').

(C''',D') Bar plot of average ZO-1b cluster area for the conditions described in (C and D). Data are shown as box-and-whisker plots (Whiskers: Tukey). Average Area of (C') with unpaired t test, *p = 0.0388. GFP-ZO-1b with N=6, n=10 embryos; GFP-ZO-1bΔABR with N=5, n=14 embryos. Average area of (D') with unpaired t test, *p = 0.0121. DMSO ctrl with N=4, n=8 embryos; LatB with N=4, n=9 embryos.

(C'''',D'') Bar plot of average ZO-1b cluster circularity for the conditions described in (C and D). Data are shown as box-and-whisker plots (Whiskers: Tukey). Circularity of (C'') with unpaired t test *p = 0.0158. GFP-ZO-1b with N=6, n=10 embryos; GFP-ZO-1bΔABR with N=5, n=12 embryos. Circularity of (D'') with Mann-Whitney test, ***p=0.0004. DMSO ctrl with N=4, n=6 embryos; LatB with N=4, n=9 embryos.

(E) Stills of a movie showing MIP high-resolution (Airy Scan) images of Tg(*actb1:mNEONgreen-zfTjp1b*) embryos treated for 1h with 1 µg/ml Latrunculin B prior to imaging at 5.3-6.3 hpf. ZO-1b clusters are frequently fusing after Latrunculin B treatment. Scale bar, 1 µm.

Figure 6. Mechanosensitive response of ZO-1b is dependent on its C-terminus
(A,B,C) Maximum intensity projections (MIPs) of GFP-tagged ZO-1b (A), GFP-tagged ZO-1b-ΔC (B) and GFP-tagged ZO-1b-ΔABR (C) localization at the EVL-YSL boundary in MZ*zo-1b/3* embryos injected with H2A-mCherry (ctrl - 2.3-2.5 pg H2A-mCherry; A with N=5, n=23 cells; B with N=4, n=43 cells; C with N=3, n=17 cells; left two columns) and embryos injected with caRhoA (0.3-0.5 pg caRhoA plus 2 pg H2B-GFP) specifically within the YSL (A with N=3, n=19 cells; B with N=3, n=13 cells; C with N=3, n=27 cells; right two columns) at the onset of

imaging (7 hpf) (0 min; 1st and 3rd column) and 24 min later (2nd and 4th column). Scale bar, 10 μm.

(A',B',C') Plot of EVL-YSL junctional intensity normalized to EVL-EVL junctional intensity as a function of time during EVL epiboly in the conditions described in (A,B,C). Data are mean ± s.e.m.

(D,E) MIPs of brightfield/fluorescence images of embryos injected directly into the YSL at high stage (3.3 hpf) with phenol red and H2A-mcherry mRNA (ctrl in D with N=8, n=27 embryos, ctrl in E with N=3, n=10 embryos), *zo-1b/3* MO (1.5 ng *zo-1b* MO, 0.5ng *zo-3* MO, D with N=8, n=28 embryos; E with N=3, n=12 embryos) alone, *zo-1b/3* MO together with *GFP-zo-3* (5 pg) and GFP-*zo-1b* (25 pg) mRNA (D with N=8, n=27 embryos; E with N=3, n=8 embryos), and *zo-1b/3* MO together with *GFP-zo-3* (5 pg) and GFP-*zo-1b*-**Δ**C (15 pg) mRNA (N=8, n=26 embryos) (D) or *zo-1b/3* MO together with *GFP-zo-3* (5 pg) and GFP-*zo-1b*-**Δ**ABR (22 pg) mRNA (N=3, n=8 embryos) (E) at 9 hpf. Plasma membrane is marked by membrane-RFP to outline cells. EVL-YSL boundary is marked by white dashed line to demarcate extent of EVL epiboly in the different conditions. Scale bar, 100 μm.

(D',E') Plot of total time required for EVL to complete epiboly for the conditions shown in (D,E) and normalized to average time needed by control embryos. Data are shown as box-and-whisker plots (Whiskers: Tukey). One-way ANOVA with ****$p < 0.0001$; ns, non significant. For full-length rescue (Figure 6D-D') , data shown in Figure 2B' were included.
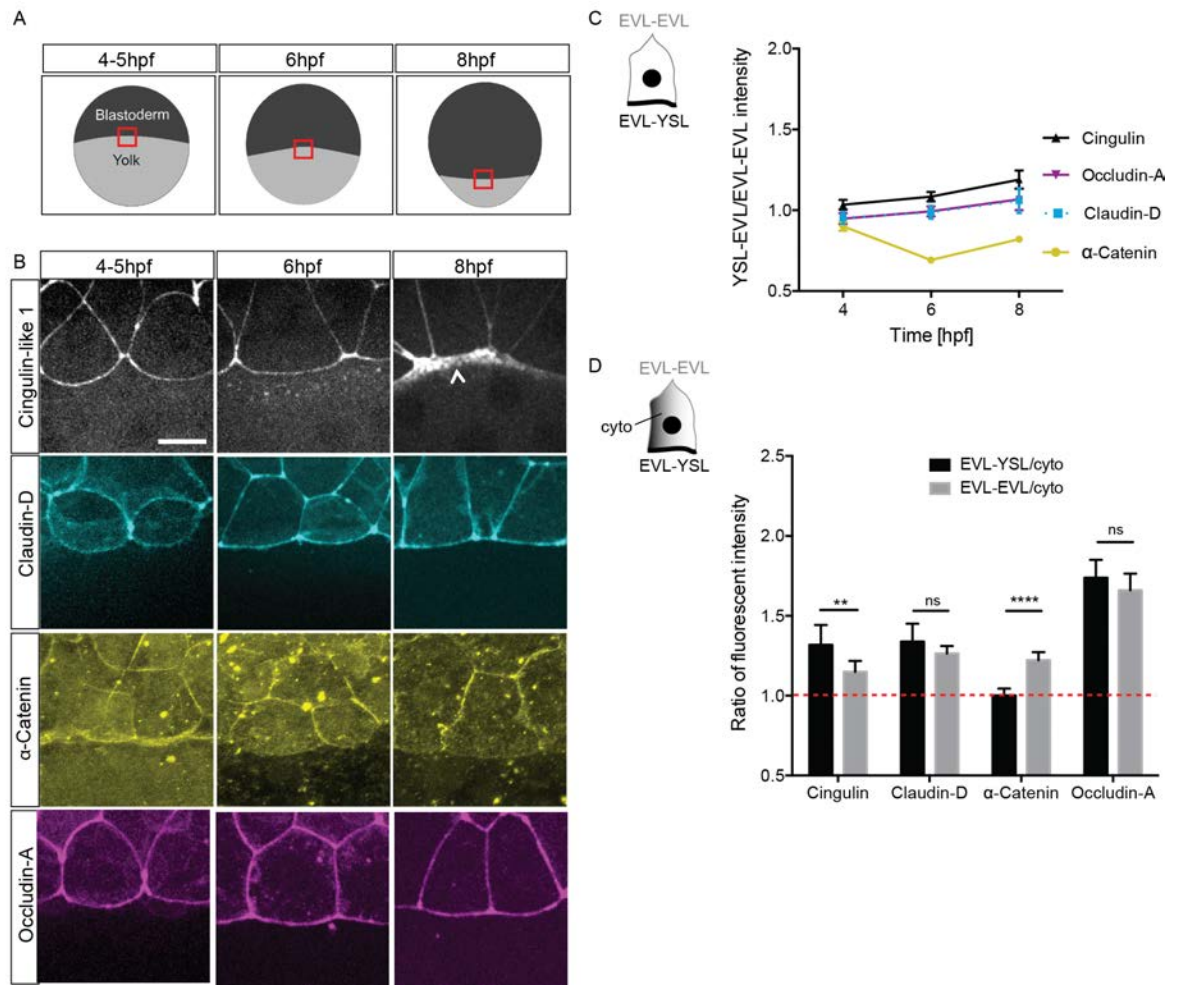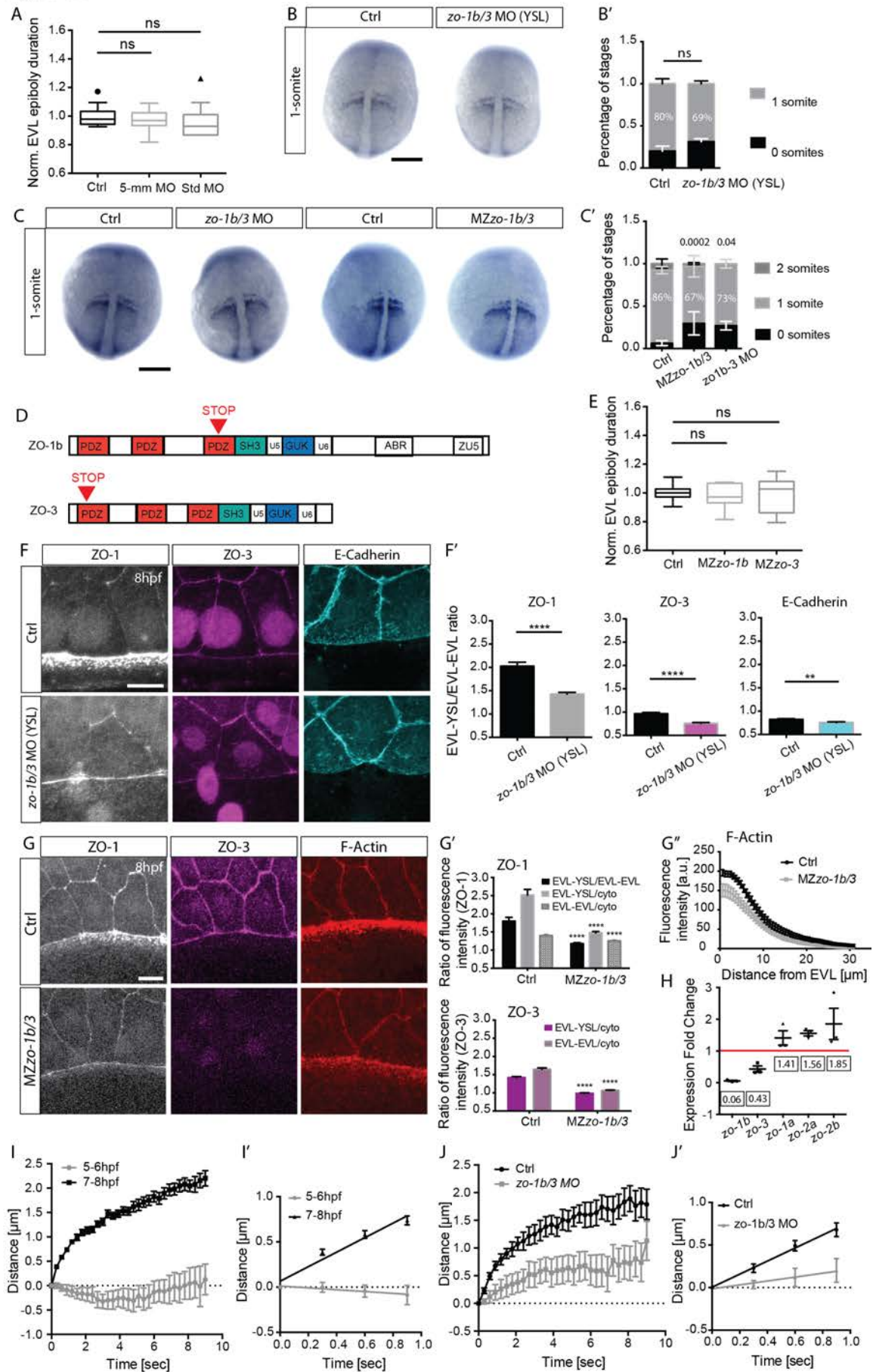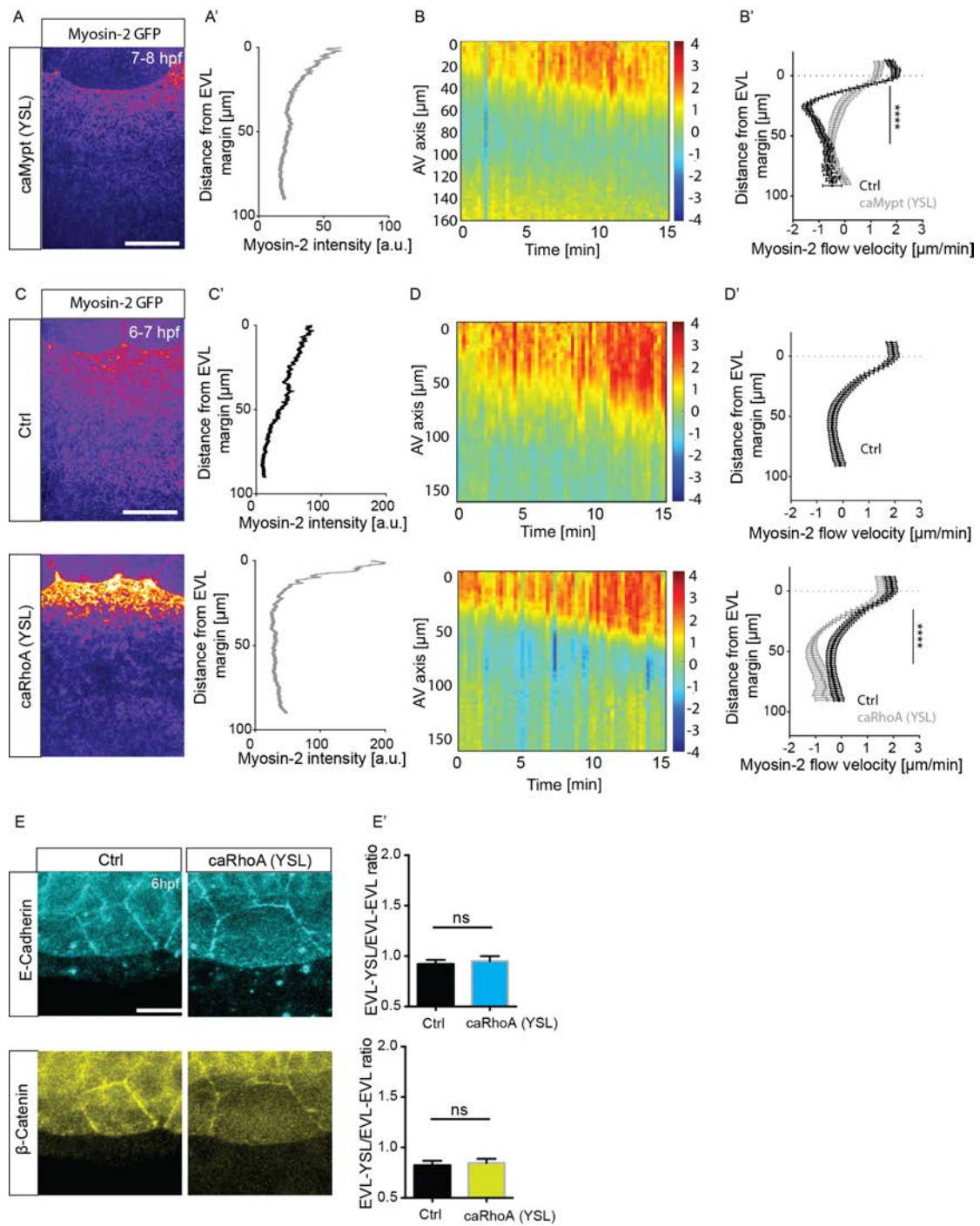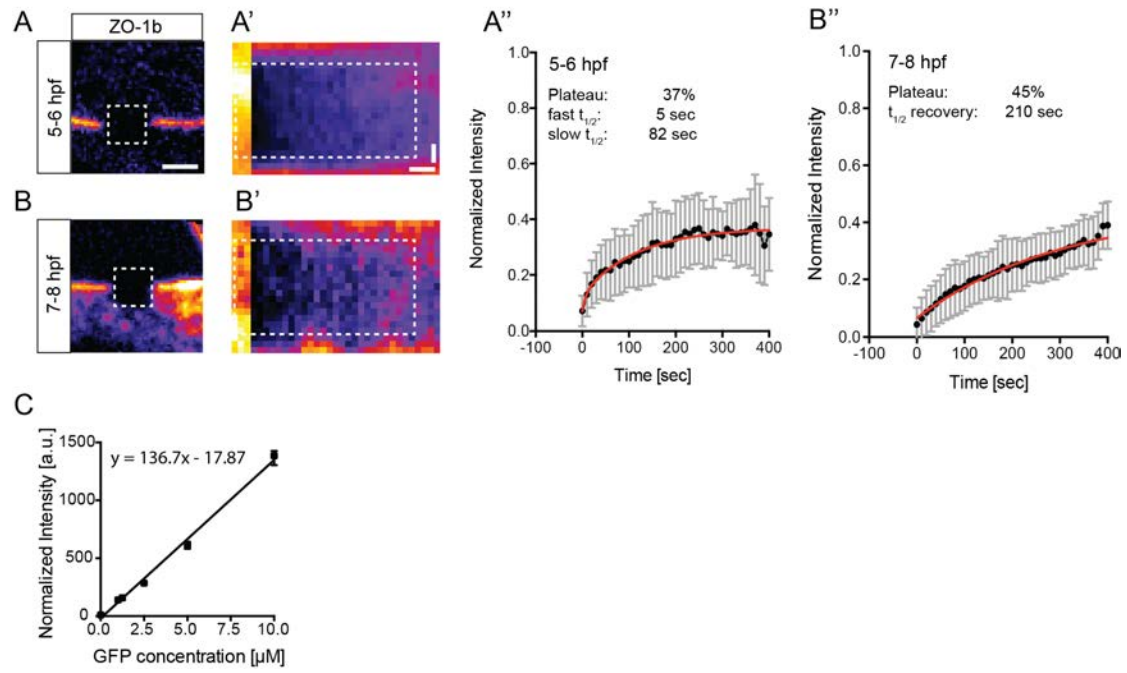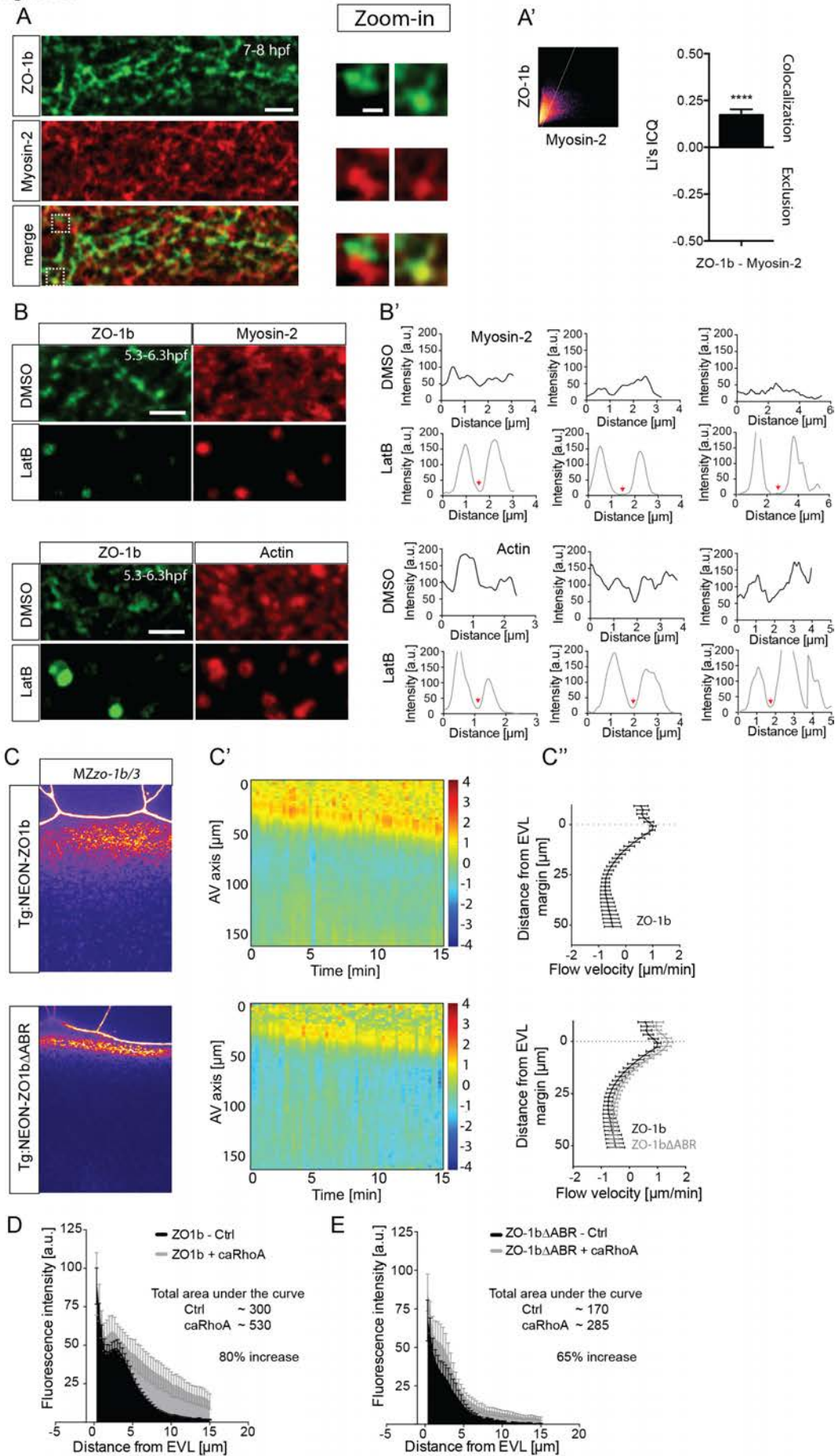
Figure S1

Figure S2

Figure S3

Figure S4

Figure S5

Figure S6

A

MZzo-1b/3 | ZO-1b | ZO-1b ΔC | 7 hpf

A'

Total Intensity [a.u.] — ns
ZO-1b, ZO-1bΔC

B

$J_{ie} = J_{ie} (J_i - J_d)$

Junctional integration efficiency J_{ie}

Junctional integration efficiency — **
ZO-1b, ZO-1bΔABR

C

MZzo-1b/3 | ZO-1b | 0'' | 105''

MZzo-1b/3 | ZO-1bΔABR | 0'' | 495'' | 0'' | 285''

C'

ZO-1b | 0'' | 45'' | 75'' | 90'' | 105''

ZO-1bΔABR | 375'' | 390'' | 405'' | 420'' | 435'' | 15'' | 45'' | 75'' | 120'' | 135''

C''

0% | 11%
Distance in y from EVL-YSL junction / Distance in z from EVL-YSL junction
Junction

5% | 67%
Distance in y from EVL-YSL junction / Distance in z for EVL-YSL junction
Junction

D

F-Actin | 8hpf | Ctrl | zo-1/3 MO (YSL) | zo-1/3 MO (YSL) +zo-1bΔC | zo-1/3 MO (YSL) +zo-1bΔABR

D'

Distance from EVL margin [μm] / Fluorescence intensity [a.u.]
Ctrl
zo-1/3 MO (YSL)
+zo-1bΔC
+zo-1bΔABR

E

ZO-1b | Cingulin-like 1 | merge | 8hpf

E'

Pearson's R value — Colocalization
ZO-1b - Cingulin-like 1

F

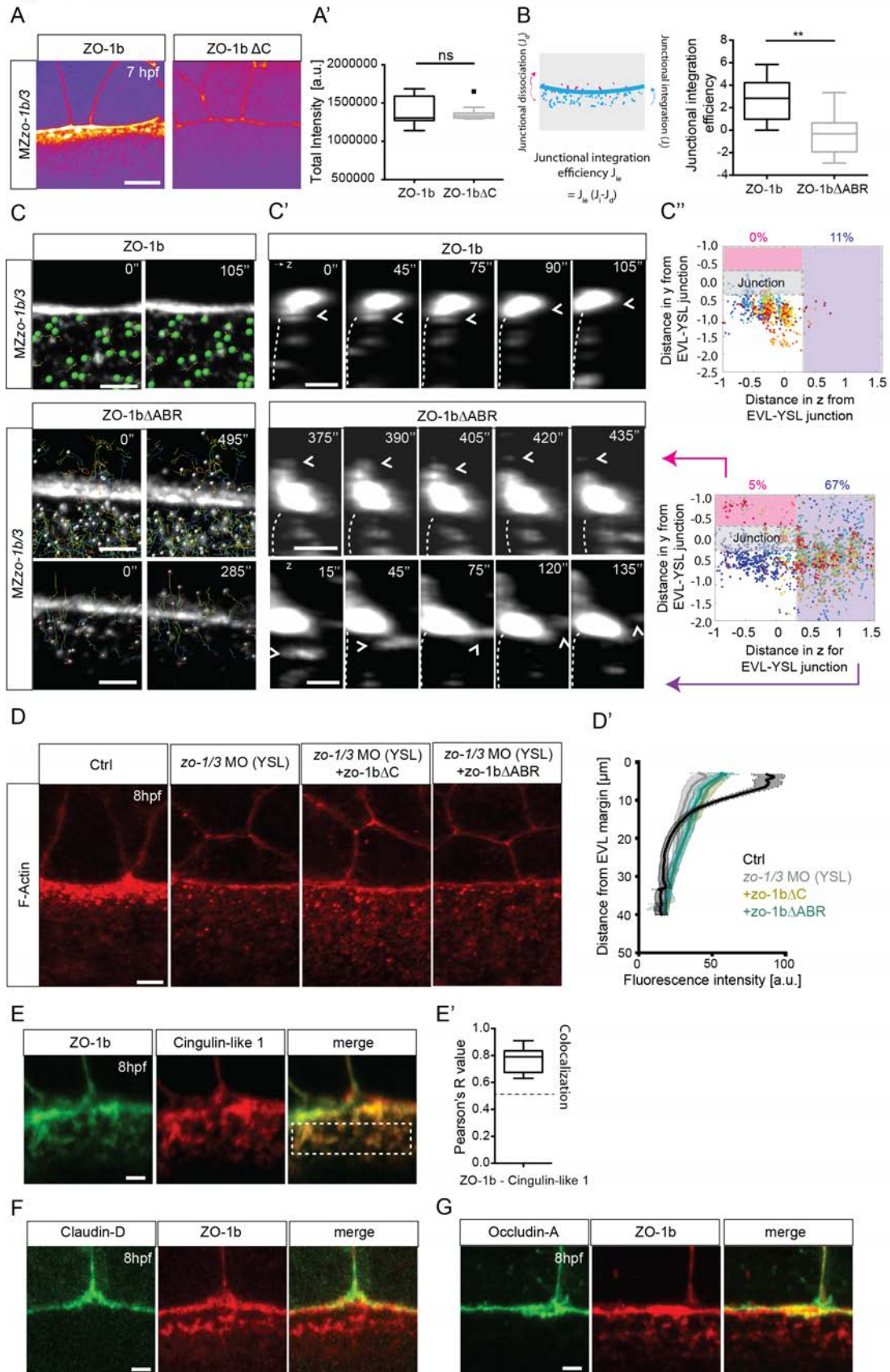Claudin-D | ZO-1b | merge | 8hpf

G

Occludin-A | ZO-1b | merge | 8hpf

Supplementary figure legends

Figure S1. Tight junction and adherens junction component accumulation at the EVL-YSL boundary

(A) Schematic representation of EVL spreading during consecutive stages of epiboly (4-5, 6 and 8 hpf). Yolk cell, light grey; blastoderm (EVL and deep cells), dark grey. Red rectangle demarcates regions of the EVL-YSL boundary shown in (B).

(B) Maximum intensity projections (MIPs) of GFP-Cingulin-like 1 (1st row), GFP-Claudin-D (2nd row), GFP-Occludin-A (3rd row) and α-Catenin (4th row) localization at the EVL-YSL boundary at 4-5 (left column), 6 (middle column) and 8 (right column) hpf. α-Catenin is visualized by immunohistochemistry, and Cingulin-like 1, Claudin-D and Occludin-A by expression of their respective GFP-fusions in wildtype embryos injected with 15 - 50 pg mRNA at 1-cell stage. White arrowheads point to increased accumulation at the EVL-YSL boundary. Scale bar, 20 µm.

(C) Plot of EVL-YSL junctional intensity normalized to EVL-EVL junctional intensity as a function of time during EVL epiboly (see also schematic above). Data are mean at 95% confidence. Cingulin-like 1 with N=2 and n=33 cells at 4-5 hpf, n=37 cells at 6 hpf and n=31 cells at 8 hpf. Claudin-D with N=2, n=40 cells at 4-5 hpf, n=50 cells at 6 hpf, n=29 cells at 8 hpf. α-Catenin with N=2 and n=45 cells at 4-5 hpf, n=29 cells at 6 hpf, n=28 cells at 8 hpf. Occludin-A with N=2, n=27 cells at 4-5 hpf; N=2, n=54 cells at 6 hpf; N=3, n=43 cells at 8 hpf.

(D) Plot of EVL-YSL junctional intensity (black) and EVL-EVL junctional intensity (grey) normalized to cytoplasmic intensity at 8 hpf. Red dashed line indicates ratio of 1 demarcating the boundary between accumulation (>1) and depletion (<1). Data are mean at 95 % confidence. Cingulin-like 1 with N=2 and n=30. Claudin-D with N=2 and n=29 cells. Occludin-A with N=3, n=43 cells. α-Catenin with N=2 and n=28 cells. Cingulin, Claudin-D and Occludin-A with Mann-Whitney test with **p = 0.0073, ns, not significant; α-Catenin, Unpaired t test with ****p < 0.0001.

Figure S2. *zo-1b/3* mutant and morphant analysis

(A) Plot of EVL tissue spreading, expressed as EVL height (h_{EVL}) normalized to total embryo height (h_{TOT}) as a function of time normalized to the average time needed by control embryos injected with either phenol-red (YSL-ctrl), *zo-1b/3* 5-base mismatch control MO (*zo1b/3* MO) or standard negative control MO (standard control MO) into the YSL. Data are mean ± s.e.m. Kruskal-Wallis test with Dunn's multiple comparisons test. ns, not significant.

Ctrl with N=4, n=14 embryos; *zo-1b/3* MO with N=3, n=12 embryos; standard control MO with N=3, n=11 embryos.

(B) Dorsal view of YSL-injected control (phenol-red, YSL-ctrl) and *zo-1b/3* morphant (YSL-morphant) embryos at 1-somite stage (10.5 hpf) labeled by in situ hybridization for *papc* outlining the forming somites. Scale bar, 200 µm.

(C) Dorsal view of control (phenol-red, ctrl) and *zo-1b/3* morphant embryos (morphant) injected at the one-cell stage, and of wild-type (wt) and MZ*zo-1b/3* mutant embryos labeled at 10.5 hpf by in situ hybridization for *papc* outlining the forming somites. Scale bar, 200 µm.

(B',C') Bar plot of stage distribution (categorized in 0, 1 and 2-somite stages as revealed by *papc* in situ hybridization) for the conditions described in (B and C). Data are mean ± s.e.m. Cumulative link mixed model (Christensen 2018) was used to determine p-values. P-values are mentioned above the columns. The percentage of embryos at 1-somite stage is indicated within the bars of the different conditions. (B') YSL-ctrl with N=3, n=36 embryos; YSL-morphant with N=3, n=45 embryos; (C') Ctrl with N=2, n=26 embryos; morphant with N=3, n=43 embryos; wt with N=4, n=72 embryos and mutant with N=5, n=77 embryos.

(D) Mutation sites in *zo-1b* and *zo-3* mutants. Red triangles indicate the insertion sites of the STOP codon.

(E) Plot of EVL tissue spreading, expressed as height of EVL (h_{EVL}) normalized to total embryo height (h_{TOT}), as a function of time normalized to average time needed by control embryos shown for wild-type (wt) control, and MZ*zo-1b* and MZ*zo-3* single mutants. Data are mean ± s.e.m. One-way ANOVA with Tukey's multiple comparisons test. ns. not significant. Wt control (Ctrl) with N=4, n=27 embryos; MZ*zo-1b* with N=3, n=16 embryos; and MZ*zo-3* with N=3, n=18 embryos.

(F) Maximum intensity projections (MIPs) of ZO-1 (left column), ZO-3 (middle column) and E-cadherin (right column) localization at the EVL-YSL boundary in YSL-Ctrl (upper row) and *zo-1b/3* YSL-morphant (lower row) embryos at 8 hpf. ZO-1, ZO-3 and E-Cadherin were detected by immunohistochemistry. Scale bar, 20µm.

(F') Plot of EVL-YSL junctional intensity normalized to EVL-EVL junctional intensity as a function of time during EVL epiboly for the conditions described in (F). Data are mean ± s.e.m. Statistical test for ZO-1 intensity with Mann-Whitney test, ****p < 0.0001; ZO-3 intensity with unpaired t test, ****p < 0.0001; and E-Cadherin intensity with unpaired t test with **p = 0.0029; ZO-1: N=2, YSL-ctrl with n=30 cells and *zo-1b/3* YSL-morphant with n=40

cells; ZO-3: N=2, YSL-ctrl with n=42 cells and *zo-1b/3* YSL-morphant with n=59 cells. E-Cadherin: N=3, ctrl with n=51 cells and *zo-1b/3* YSL-morphant with n=54 cells.

(G) MIPs of ZO-1 (left column), ZO-3 (middle column) and F-actin (right column) localization at the EVL-YSL boundary in wt (upper row - Ctrl) and MZ*zo-1b/3* mutant (lower row) embryos at 8 hpf. ZO-1 and ZO-3 were detected by immunohistochemistry, and F-actin by Phalloidin. ZO-1 antibody likely detects both zebrafish ZO-1a and ZO-1b, suggesting that the remaining signal in the MZ*zo-1b/3* mutant reflects ZO-1a protein expression.

(G') Plot of EVL-YSL junctional intensity normalized to EVL-EVL junctional intensity, and EVL-YSL junctional intensity together with EVL-EVL junctional intensity normalized to cytoplasmic intensity at 8 hpf for the conditions shown in (G). Data are mean ± s.e.m. Statistical test for ZO-1: EVL-YSL/EVL-EVL with Mann-Whitney test ****$p < 0.0001$, and EVL-YSL/cyto and EVL-EVL/cyto with unpaired t-test with ****$p < 0.0001$; ZO-3: EVL-YSL/cyto and EVL-EVL/cyto with unpaired t-test with ****$p < 0.0001$. N=2, wt with n=31 cells and MZ*zo-1b/3* mutant with n=33 cells.

(G'') Plot of F-Actin fluorescence intensity within the YSL as a function of distance from EVL margin for the conditions described in (D). F-actin was detected by Phalloidin. [a.u.], arbitrary units. N=2, wt with n=7 embryos and MZ*zo-1b/3* mutant with n=7 embryos.

(H) Compensatory expression changes of *zo* genes in MZ*zo-1b/3* mutant embryos normalized to the expression level of a housekeeping gene (*elongation factor 1α*). Fold change reflects the relative change of expression levels in MZ*zo-1b/3* mutant compared to wt embryos in qRT-PCR. Red solid line indicates 1-fold change in expression, demarcating the boundary between increase (>1) and decrease (<1) of expression levels of the five different *zo* genes (N=3, n=triplicates each).

(I,J) Plot of junctional opening (distance in μm) of the EVL-YSL boundary marked by Myosin-2-GFP after UV laser cutting at mid (6 hpf) and late (8 hpf) stages of EVL epiboly in wt (I) and YSL-ctrl and *zo-1b/3* YSL-morphant (J) as a function of time after cutting.

(I',J') Plot of the first four time-points from (I,J) with linear fit to extract initial recoil velocity shown in (Figure 2E'', 2F''). N,n see (Figure 2E-F).

Figure S3. Effects of actomyosin contractility and flow on TJ and AJ protein recruitment to EVL-YSL boundary

(A,C) MIPs of Myosin-2 localization at the EVL-YSL boundary in Tg(*actb1:myl12.1-eGFP*) embryos that were either injected into the YSL at high stage (3.3 hpf) with caMypt (75pg caMypt plus 25pg H2A-mcherry, right column) shown at 8 hpf (A), or injected into marginal

blastomeres/YSL at 128-cell stage with H2B-EGFP (2.3-2.5 pg - left column, ctrl) and caRhoA mRNA (0.3-0.5 pg caRhoA plus 2 pg H2B-GFP, right column) shown at 6 hpf (C). Scale bar, 20μm.

(A'C') Plot of Myosin-2 intensity as a function of distance from EVL margin in an exemplary caMypt (A'), ctrl and caRhoA (C') YSL-injected embryo at 7-8 hpf and 6-7 hpf, respectively. [a.u.] arbitrary units.

(B,D) Kymograph of Myosin-2 flow velocities along the animal-vegetal (AV) axis of the embryo as a function of time during epiboly in an exemplary caMypt (B), Ctrl and caRhoA YSL-injected embryo embryo (D) at 7-8 hpf and 6-7 hpf, respectively. Kymograph ranges from negative values (in blue), indicating retrograde flows towards the EVL margin, to positive values (in red), indicating anterograde flows towards the vegetal pole.

(B',D') Plot of Myosin-2 mean flow velocities along AV axis averaged over 10-30 min in caMypt (B'), Ctrl and caRhoA (D') YSL-injected embryos between 7-8 hpf and 6-7 hpf, respectively. EVL and YSL peak velocities averaged over 10 μm and 45 μm (15 - 60 μm from EVL margin), respectively. Statistical test for caMypt, Mann-Whitney test, ****p < 0.0001. Statistical test for caRhoA, Unpaired t test, ****p < 0.0001. For N/n of YSL-ctrl see (Figure 2D'). caMypt YSL injected embryos with N=3, n=5 (B'); ctrl with N=2, n=6 and caRhoA with N=3, n=5 (D').

(E) Maximum intensity projections (MIPs) of E-Cadherin (1st column) and β-Catenin (2nd column) localization at the EVL-YSL boundary in uninjected control embryos (ctrl; first row) and embryos injected into the YSL with caRhoA (0.3-0.5 pg caRhoA plus 2pg H2B-EGFP) mRNA at 6 hpf (second row). E-Cadherin and β-Catenin were detected by immunohistochemistry. Scale bar, 20μm.

(E') Plots of E-cadherin and β-Catenin intensities at the EVL-YSL boundary normalized to EVL-EVL junctional intensity for the conditions described in (E). Mann-Whitney test, ns, not significant; E-cadherin and β-Catenin with N=2, control with n=31 cells and caRhoA injected embryos with n=27 cells.

Figure S4. Junctional ZO-1b dynamics
(A,B) Sum intensity projection image (sum of all slices) of GFP-ZO-1b signal in Tg(*actb1:mNEONgreen-zfTjp1b*) embryos at the EVL-YSL boundary (A with N=3, n=9 cells and B with N=2, n=10 cells) after bleaching in FRAP experiments at early-mid (5-6 hpf; A) and late epiboly stage (7-8 hpf; B). White dashed box outlines bleached region. Scale bar, 5 μm.

(A',B') Exemplary kymograph of bleached region for the conditions described in (A,B). White dashed box outlines region used for intensity measurements. Horizontal scale bar, 40 s; vertical scale bar, 1 μm.

(A",B") Plot of GFP-ZO-1b fluorescence recovery as a function of time for the conditions described in (A,B). Data are mean ± SD. Intensity values were normalized to the pre-bleach intensities and to reference junctional signals to correct for bleaching (more details see Materials and Methods). Solid line shows a double exponential fit (A'') and single exponential fit (B'').

(C) Calibration curve of fluorescence intensity normalized to laser power as a function of GFP protein concentration. a.u., arbitrary units. PBS with N=3; 1 μM with N=1; 1.25 μM with N=2; 2.5 μM with N=2; 5 μM with N=2; 10 μM with N=3.

Figure S5. Interaction of ZO-1b and the actomyosin network within the YSL

(A) Single plane fluorescence images of ZO-1b, Myosin-2 and an overlay of ZO-1b and Myosin-2 to visualize ZO-1b/Myosin-2 protein co-localization within the YSL of Tg(*actb1:myl12.1-mcherry*; *actb1:mNEONgreen-zfTjp1b*) embryos at 6-8 hpf. White boxes demarcate zoom-in region of examples of either mutual exclusive localization or co-localization of ZO1b and Myosin-2. Scale bar, 2 μm (left panel) and 0.5 μm (right panel).

(A') Scatterplot of ZO-1b and Myosin-2 showing a wide signal spread implying partial colocalization (for more details see Material and Methods). Bar plot of Li's Intensity Correlation Quotient (ICQ) for colocalization quantification of ZO-1b and Myosin-2 between 6-8 hpf. Li's ICQ value ranges from 0.5 showing colocalization to -0.5 showing exclusion and values close to 0 indicate random localization. N=4, n=17 embryos.

(B) Maximum intensity projections (MIPs) of ZO-1b, Myosin-2 and Actin signals within the YSL of Tg(*actb1:myl12.1-mcherry*; *actb1:mNEONgreen-zfTjp1b*) *and Tg(actb2:NeonGreen-zfTjp1b) (actb2:Utrophin-mcherry)* embryos exposed for 1h to DMSO (control) and 1 μg/ml Latrunculin B from 5.3 to 6.3hpf. Scale bar, 2 μm.

(B') Line plots of Myosin-2 and Actin network intensity distribution within the YSL of three exemplary embryos each upon DMSO and Latrunculin B treatment. Note the strong decrease in signal between two Myosin-2 or Actin clusters upon Latrunculin B treatment (indicated with red arrow heads).

(C) MIPs of ZO-1b and ZO-1b-**Δ**ABR at the EVL-YSL boundary in *Tg(actb2:NeonGreen-zfTjp1b) and Tg(actb2:NeonGreen-zfTjp1b***Δ**ABR) transgenic MZ*zo-1b/3* mutant embryos at 7-8 hpf. Scale bar, 20μm.

(C') Kymograph of flow velocities of ZO-1b and ZO-1b-**Δ**ABR along the animal-vegetal (AV) axis of the embryo as a function of time during epiboly in exemplary embryos at 7-8 hpf. Kymograph ranges from negative values (in blue), indicating retrograde flows towards the EVL margin, to positive values (in red), indicating anterograde flows towards the vegetal pole.

(C'') Plot of Myosin-2 mean flow velocities along AV axis averaged over 10-30 min for the conditions described in (C) between 7 and 8 hpf. ZO-1b with N= 3, n=4 embryos, ZO-1b-**Δ**ABR with N=3, n=8 embryos.

(D,E) Plot of non-junctional fluorescence intensity of full-length ZO-1b (D) and ZO-1b-**Δ**ABR (E) as a function of distance from the EVL margin in control embryos and embryos overexpressing caRhoA within the YSL. Data are mean ± s.e.m. Full-length ZO-1b: ctrl with N=5, n=6 embryos and caRhoA with N=3, n=6 embryos. ZO-1b-**Δ**ABR: ctrl with N=3, n=5 embryos and caRhoA with N=3, n=6 embryos.

Figure S6. Mechanosensitive responses of TJ proteins

(A) Sum intensity projections (SUM) of GFP-ZO-1b and GFP-ZO-1bΔC localization in MZ*zo-1b/3* mutant embryos at the EVL-YSL boundary at 8 hpf. Scale bar 20 μm.

(A') Total intensity measurement normalized to laser power for the conditions described in (A). Data are shown as box-and-whisker plots (Whiskers: Tukey). Mann Whitney test; ns, not significant. ZO-1b with N=2, n=20 embryos; ZO-1bΔC with N=2, n=21 embryos.

(B) Sketch of how junctional integration efficiency (J_{ie}) was calculated: number of clusters merging and integrating with the EVL-YSL junction (J_i) subtracted by the number of clusters dissociating from the junction (J_d) and leaving towards the internal or external YSL. Bar plot shows quantification of junctional integration efficiency normalized to a 3 min time window.

(C) Maximum intensity projections (MIPs) of ZO-1b and ZO-1b**Δ**ABR in MZ*zo-1b/3* mutant embryos at the first time point of tracking and the last time point of tracking non-junctional clusters. Scale bar, 2 μm.

(C') MIPs of yz-plane of ZO-1b and ZO-1b**Δ**ABR cluster tracking with clusters typically being incorporated into the TJ for ZO-1b, and flowing below the TJ into the internal YSL or detaching from the junctional pool for ZO-1b**Δ**ABR. White dashed line indicates apical side of YSL facing the outside. Scale bar, 1 μm (1st and 3rd row). Scale bar, 2 μm (2nd row).

(C'') Tracks of non-junctional clusters for the conditions described in (C). Region shaded in grey outlines the EVL-YSL junction in yz direction; region shaded in pink outlines region above the EVL-YSL junction, where usually almost no cluster leaves in the ZO-1b case but ZO-

1b ABR shows clusters that detach from the junction (11%); region shaded in lilac shows clusters further away from apical actomyosin-rich side (compare 67% in ZO-1b*Δ*ABR vs. 11% in ZO-1b case). ZO-1b with N=2, n=3; ZO-1b*Δ*ABR with N=3, n=3.

(D) MIPs of F-Actin (Phalloidin) of YSL-Ctrl (phenol red injected), *zo-1b/3* YSL-morphant (1.5ng, 0.5 ng into the YSL) and *zo-1b/3* YSL-morphant embryos co-injected with GFP-tagged *zo-1bΔ*C (15 pg) and *zo-3* (5 pg, mutated for MO recognition site) as well as GFP-tagged *zo-1bΔ*ABR (22 pg) and *zo-3* mRNAs at 8 hpf. Scale bar, 10 µm.

(D') Plot of F-Actin intensity as a function of distance from EVL margin for the conditions described in (D).

(E) MIPs of GFP-tagged ZO-1b and mcherry-tagged Cingulin-like 1 co-localization at the EVL-YSL boundary. Scale bar, 2µm.

(E') Co-localization analysis (Pearson's R value) of GFP-tagged ZO-1b (50 pg) and mcherry-tagged Cingulin-like 1 (100 pg) in wildtype (wt) embryos at 8 hpf. Pearson's R value = 0.8, indicating strong co-localization between the two proteins. N=3, n=9 embryos.

(F) MIPs of GFP-tagged Claudin-D (30 pg) and mcherry-tagged ZO-1b (70 pg) localization at the EVL-YSL boundary. Scale bar, 2µm.

(G) MIPs of mNEON-tagged Occludin-A (30-50 pg) and mcherry-tagged ZO-1b (70 pg) localization at the EVL-YSL boundary. Scale bar, 2µm.